Active and passive fields face to face

Antonio Celani, Massimo Cencini, Andrea Mazzino, Massimo Vergassola

OPEN ACCESS

Active and passive fields face to face

New Journal of Physics
An Institute of Physics and Deutsche Physikalische Gesellschaft Journal

Active and passive fields face to face

Antonio Celani[1,5], **Massimo Cencini**[2], **Andrea Mazzino**[3] **and Massimo Vergassola**[4]

[1] CNRS, INLN, 1361 Route des Lucioles, 06560 Valbonne, France
[2] Center for Statistical Mechanics and Complexity, INFM Roma 1 and Dipartimento di Fisica, Università di Roma 'La Sapienza', Piazzale Aldo Moro, 2, I-00185 Roma, Italy
[3] INFM–Dipartimento di Fisica, Università di Genova, Via Dodecaneso 33, I-16146 Genova, Italy
[4] CNRS, Observatoire de la Côte d'Azur, B.P. 4229, 06304 Nice Cedex 4, France and CNRS, URA 2171, Institut Pasteur, 28 rue du Dr. Roux, 75724 Paris Cedex 15, France
E-mail: Antonio.Celani@inln.cnrs.fr

New Journal of Physics **6** (2004) 72
Received 7 April 2004
Published 6 July 2004
Online at http://www.njp.org/
doi:10.1088/1367-2630/6/1/072

Abstract. The statistical properties of active and passive scalar fields transported by the same turbulent flow are investigated. Four examples of active scalar have been considered: temperature in thermal convection, magnetic potential in two-dimensional (2D) magnetohydrodynamics (MHD), vorticity in 2D Ekman turbulence and potential temperature in surface flows. In the cases of temperature and vorticity, it is found that the active scalar behaviour is akin to that of its co-evolving passive counterpart. The two other cases indicate that this similarity is in fact not generic and differences between passive and active fields can be striking: in 2D MHD, the magnetic potential performs an inverse cascade, whereas the passive scalar cascades towards the small scales; in surface flows, although both perform a direct cascade, the potential temperature and the passive scalar have different scaling laws already at the level of low-order statistical objects. These significant differences are rooted in the correlations between the active scalar input and the particle trajectories. The role of such correlations in the issue of universality in active scalar transport and the behaviour of dissipative anomalies is addressed.

[5] Author to whom any correspondence should be addressed.

PII: S1367-2630(04)79053-9

Contents

1. Introduction

Scalar fields transported by turbulent flows are encountered in many natural phenomena and in engineering problems ranging from atmospheric physics [1] and combustion [2] to the transport and amplification of magnetic fields in astrophysical fluids [3]. In this paper, we consider the case of advected scalar fields such as temperature, pollutant density and chemical or biological species concentration.

In many cases, there is a two-way coupling between the scalar and the flow: the transported field can influence the velocity field—this is dubbed *active* transport. This is the case, for example, of the temperature field that acts on velocity through buoyancy forces. Conversely, situations where the feedback of the scalar field is negligible and the velocity determines the properties of the scalar, but not vice versa, are termed *passive*. This ideal case is well approximated by the use of fluorescent dye in laboratory experiments to mark fluid parcels.

Although active and passive scalars are governed by the same advection–diffusion equation, their nature is radically different. Passive scalars belong to the realm of linear problems, despite being highly nontrivial. Indeed, as a consequence of the statistical independence of the forcing and the advecting velocity, the transported field depends linearly on the forcing. This property allows a fully fledged theoretical treatment of the problem, and has the major consequence that

the passive scalar scaling laws are universal with respect to the injection mechanism. On the contrary, for active fields, the presence of the feedback couples the velocity with the transported scalar and makes the problem fully nonlinear. In this case, the theoretical tools developed for studying the passive problem may fall short of explaining the behaviour of active scalars, and the current understanding of active turbulent transport lags far behind the knowledge accumulated on the passive counterpart. This state of the art motivated us to pursue a 'case study' on turbulent transport of active and passive scalars using the scaling properties of fields evolving in the same turbulent flow as the basic diagnostics for comparison.

We consider four different systems belonging to the following general classes of problems: (i) active scalars that influence the flow through local forces; and (ii) active fields functionally related to the velocity.

The evolution of a scalar belonging to the first class is described in terms of the following set of equations:

$$\partial_t a + \boldsymbol{v} \cdot \nabla a = \kappa \Delta a + f_a, \tag{1}$$

$$\partial_t c + \boldsymbol{v} \cdot \nabla c = \kappa \Delta c + f_c, \tag{2}$$

$$\partial_t \boldsymbol{v} + \boldsymbol{v} \cdot \nabla \boldsymbol{v} = -\nabla p + \nu \Delta \boldsymbol{v} + \boldsymbol{F}[a, \nabla a, \ldots], \tag{3}$$

where a and c are the active and passive scalar fields, respectively, and obey the advection–diffusion equations (1) and (2). The scalar inputs f_a and f_c have a characteristic lengthscale ℓ_f, and represent two different realizations of the same stochastic process. Were they coincident, no difference between active and passive fields would persist. For the sake of simplicity, we use the same molecular diffusivity κ for both scalars. The active character of a is embodied by the term $\boldsymbol{F}[a, \nabla a, \ldots]$, which acts as a forcing for the velocity field in the Navier–Stokes equations. The specific form of the term $\boldsymbol{F}$ depends on the physical system under investigation. In the following, we shall consider two examples from this class: thermal convection [4, 5], where a is the temperature field and $\boldsymbol{F} = -\beta a \boldsymbol{g}$ the buoyancy force, and two-dimensional (2D) magnetohydrodynamics (MHD) [6], where a the magnetic potential and $\boldsymbol{F} = -\Delta a \nabla a$ the Lorentz force.

The second class of active scalars is relevant to geophysical flows [7, 8]. In this case, the dynamics is described in terms of a scalar field obeying the advection–diffusion equation (1), supplemented by a functional relation that gives $\boldsymbol{v}$ in terms of a:

$$v_i(\boldsymbol{x}, t) = \int \Gamma_i(\boldsymbol{x} - \boldsymbol{y}) a(\boldsymbol{y}, t)\, \mathrm{d}\boldsymbol{y}. \tag{4}$$

Here, the vector-valued kernel $\boldsymbol{\Gamma}$ is divergence-free. A well-known instance from such a class is the 2D Navier–Stokes equation, where the active scalar is the vorticity $\nabla \times \boldsymbol{v}$. Another problem which we shall discuss is the turbulent flow on the flat surface of an infinitely high fluid, described by the surface-quasi-geostrophic equation [9, 10]. Here, the active scalar is the fluid density, which is related (e.g. for ideal gases) to the so-called potential temperature.

Some of the results presented in this paper were discussed previously in [11]–[13]. Related investigations on active and passive transports may be found in [14]–[17].

This paper is organized as follows. In section 2, we briefly review some results about passive scalar transport in turbulent flows. Particular emphasis is put on the Lagrangian description of scalar transport, pointing out the results which hold for active scalars as well. In section 3, the

statistics of the (active) temperature and a passive scalar field in 2D convection is discussed. Section 4 is devoted to the analysis of 2D MHD, with a thorough discussion of the problem of dissipative anomaly in scalar transport. In section 5, the evolution of passive and active fields in Ekman–Navier–Stokes turbulence is discussed. In section 6, we study the properties of turbulence on fluid surfaces under the quasi-geostrophic approximation. In the last section, we summarize the main findings and delineate the perspectives for active scalar transport.

2. Passive scalar turbulence

2.1. Eulerian approach

The dynamics of passive scalars is governed by the advection–diffusion equation (2). To describe the general properties of passive scalar evolution in turbulent incompressible velocity fields, we assume that the velocity field $\boldsymbol{v}$ is scale-invariant and rough. In other words, the spatial increments $\delta_r v = (\boldsymbol{v}(\boldsymbol{x}+\boldsymbol{r},t) - \boldsymbol{v}(\boldsymbol{x},t)) \cdot \boldsymbol{r}/r$ depend on the separation r as a fractional power, i.e. $\delta_r v \sim r^h$ with $h < 1$ (e.g. $h = 1/3$ in Kolmogorov's 1941 turbulence [18]). Being interested in the statistically steady properties of the field, we introduce a source of scalar fluctuations f_c. In the following, we take for convenience a random, Gaussian, statistically homogeneous and isotropic forcing with zero mean and correlation function

$$\langle f_c(\boldsymbol{x}_1,t) f_c(\boldsymbol{x}_2,t')\rangle = \delta(t-t')\mathcal{F}(|\boldsymbol{x}_1-\boldsymbol{x}_2|/\ell_f). \tag{5}$$

The correlation function of the forcing $\mathcal{F}(r/\ell_f)$ is roughly constant at scales smaller than ℓ_f, which is assumed to be within the scaling range of $\boldsymbol{v}$, and decreases rapidly to zero for $r > \ell_f$.

The phenomenology of passive scalar turbulence may be summarized as follows. Scalar fluctuations injected at the scale ℓ_f are transferred towards the small scales with a constant flux down to the dissipative scale ℓ_d. There, the molecular diffusion absorbs the incoming flux and ensures the equilibrium between the input and the dissipation. The fluctuations are thus maintained in a statistically steady state, which is characterized by two major properties. First, the scalar dissipation is asymptotically independent of the molecular diffusivity κ, attaining a finite non-zero limiting value for $\kappa \to 0$. This singular behaviour of the dissipation is also known as *dissipative anomaly*. Second, in the scaling range $\ell_d \ll r \ll \ell_f$, the scalar statistics is *intermittent*. This amounts to saying that the small-scale statistics is characterized alternation between strong, rare events, where scalar increments $\delta_r c = c(\boldsymbol{x}+\boldsymbol{r},t) - c(\boldsymbol{x},t)$ are much larger than their typical value, c_{rms}, and long quiescent phases, where $\delta_r c \ll c_{rms}$. Intermittency is reflected by the scaling behaviour of the structure functions, i.e. the moments of the scalar increments

$$S_N^c(r) = \langle (\delta_r c)^N \rangle \propto r^{\zeta_N^{dim}} \left(\frac{\ell_f}{r}\right)^{\zeta_N^{dim}-\zeta_N^c}. \tag{6}$$

The scaling exponents ζ_N^c are said to be *anomalous* when they deviate from the dimensional expectation $\zeta_N^{dim} = N(1-h)/2$. The equality $\zeta_N^c = \zeta_N^{dim}$ holds probably only for $N = 2$ [4], whereas for $N > 2$, the deviations become increasingly severe. The asymptotic behaviour at large orders N corresponds to the saturation $\zeta_N^c \to \zeta_\infty^c$ [19]. The saturation is related to the presence of sharp 'fronts' in the scalar field. The exponents ζ_N^c are *universal* with respect to the details of the energy injection statistics. The forcing only affects the numerical prefactors appearing in the structure functions.

The anomalous scaling $\zeta_N^{dim} \neq \zeta_N^c$ signals the breakdown of scale invariance, as confirmed by the explicit appearance of ℓ_f in (6), even at scales $r \ll \ell_f$. Indeed, anomalous scaling of the moments of scalar increments is equivalent to state that the probability density functions (pdfs) of $\delta_r c$ at different values of r cannot be collapsed by rescaling them with a unique power law in r. Even though the specific values of the exponents ζ_N^c depend on the details of the flow (statistics, time correlation and roughness exponent h), intermittency and the breaking of scale invariance in the scalar statistics are generic features of passive scalar turbulence.

The physical mechanism leading to anomalous scaling has been recently understood in the framework of the Kraichnan model of scalar advection [20, 21] (see [22]–[25] for exhaustive reviews on the subject). In this model, the advecting flow $\boldsymbol{v}$ is random, Gaussian, self-similar and δ-correlated in time. Under these special conditions, there exists a closed set of linear equations for multi-point correlation functions. The anomalous exponents are the scaling exponents of the homogeneous solutions (the so-called *zero modes*) of those equations. Since homogeneous solutions do not depend, by definition, on the scalar input, their scaling exponents are universal and cannot be inferred from dimensional arguments. The concept of zero mode can be extended to passive scalar turbulence in generic velocity fields [26].

The properties of passive scalars described above are in the language of fields—the Eulerian description. It is of interest to adopt now a different, but equivalent viewpoint in terms of particle trajectories, namely the Lagrangian description.

2.2. *Lagrangian description*

The basic idea of the Lagrangian approach is to solve equation (2) by the method of characteristics. Let us denote $\boldsymbol{\rho}(s; \boldsymbol{x}, t)$ as the trajectory of a fluid particle landing at point $\boldsymbol{x}$ at time t (henceforth, whenever there is no ambiguity, we indicate this as $\boldsymbol{\rho}(s)$). The path $\boldsymbol{\rho}(s)$ is the solution of the stochastic differential equation

$$\frac{\mathrm{d}\boldsymbol{\rho}(s)}{\mathrm{d}s} = \boldsymbol{v}(\boldsymbol{\rho}(s), s) + \sqrt{2\kappa}\dot{\boldsymbol{w}}(s), \qquad \boldsymbol{\rho}(t) = \boldsymbol{x}, \tag{7}$$

where $i, j = 1, \ldots, d$ (d being the space dimensionality) and $\dot{\boldsymbol{w}}(s)$ is a Wiener process (the derivative of a Brownian motion), i.e. $\dot{w}_i$ are Gaussian variables of zero mean and correlation $\langle \dot{w}_i(s)\dot{w}_j(s')\rangle = \delta_{ij}\delta(s - s')$. Along the path $\boldsymbol{\rho}(s)$, equation (2) reduces to

$$\frac{\mathrm{d}\phi^{\boldsymbol{w}}(s)}{\mathrm{d}s} = f_c(\boldsymbol{\rho}(s), s), \tag{8}$$

which is easily solved as $\phi^{\boldsymbol{w}}(t) = \int_0^t \mathrm{d}s\, f_c(\boldsymbol{\rho}(s), s)$. For the sake of simplicity, we assumed $\phi^{\boldsymbol{w}}(0) = 0$. We indicated, with $\phi^{\boldsymbol{w}}$, the solution obtained along the path $\boldsymbol{\rho}$ obtained for a specific realization of the process $\boldsymbol{w}$. The passive scalar field $c(\boldsymbol{x}, t)$ is recovered by averaging over all the realizations of $\boldsymbol{w}$, i.e. along all the Lagrangian paths ending in $\boldsymbol{x}$ at time t [27]:

$$c(\boldsymbol{x}, t) = \langle \phi^{\boldsymbol{w}}(t)\rangle_{\boldsymbol{w}} = \left\langle \int_0^t \mathrm{d}s\, f_c(\boldsymbol{\rho}(s), s) \right\rangle_{\boldsymbol{w}}. \tag{9}$$

The statistic of the trajectories is summarized in the particle propagator $P(\boldsymbol{y}, s|\boldsymbol{x}, t) = \langle \delta(\boldsymbol{y} - \boldsymbol{\rho}(s; \boldsymbol{x}, t)\rangle_{\boldsymbol{w}}$, which is the probability of finding a particle at point $\boldsymbol{y}$ and time $s \leqslant t$,

provided it is in $\boldsymbol{x}$ at time t. According to the theory of stochastic processes [28], $P(\boldsymbol{y}, s|\boldsymbol{x}, t)$ obeys the Kolmogorov equations

$$-\partial_s P(\boldsymbol{y}, s|\boldsymbol{x}, t) - \boldsymbol{\nabla}_y \cdot [\boldsymbol{v}(\boldsymbol{y}, s) P(\boldsymbol{y}, s|\boldsymbol{x}, t)] = \kappa \Delta_y P(\boldsymbol{y}, s|\boldsymbol{x}, t), \tag{10}$$

$$\partial_t P(\boldsymbol{y}, s|\boldsymbol{x}, t) + \boldsymbol{\nabla}_x \cdot [\boldsymbol{v}(\boldsymbol{x}, t) P(\boldsymbol{y}, s|\boldsymbol{x}, t)] = \kappa \Delta_x P(\boldsymbol{y}, s|\boldsymbol{x}, t) \tag{11}$$

with the initial condition $P(\boldsymbol{y}, t|\boldsymbol{x}, t) = \delta(\boldsymbol{x} - \boldsymbol{y})$. The unusual minus signs on the l.h.s. of (10) are due to the fact that particles move *backward* in time. The solution of (2) can be written in terms of the propagator as

$$c(\boldsymbol{x}, t) = \int_0^t \mathrm{d}s \int \mathrm{d}\boldsymbol{y}\, f_c(\boldsymbol{y}, s) P(\boldsymbol{y}, s|\boldsymbol{x}, t), \tag{12}$$

as it can be directly checked by inserting (12) into (2) and using (11).

At variance with smooth velocities (i.e. Lipschitz continuous, $\delta_r v \sim r$), where the particle trajectories are unique for $\kappa \to 0$, the particle propagator does not collapse onto a single trajectory in the limit $\kappa \to 0$ for velocity fields rough and incompressible. Lagrangian paths are not unique and initially coincident particles separate in a finite time. This property is at the root of the dissipative anomaly.

For active and passive scalars evolving in the same flow, the Lagrangian paths $\boldsymbol{\rho}(s)$ as well as the propagator $P(\boldsymbol{y}, s|\boldsymbol{x}, t)$ are the same. The difference between a and c is that, since the active scalar enters the dynamics of $\boldsymbol{v}$ (equations (3) and (4)), the Lagrangian trajectories are functionally related to the active scalar forcing f_a, but are independent of the passive source term f_c. This is the Lagrangian counterpart of the linearity of the passive scalar problem, which does not hold for the more complicated case of active scalars.

One of the advantages of the Lagrangian description is that it makes the physics of transport processes transparent. For instance, let us consider the two-point correlation function for passive scalars, $\mathcal{C}^c(\boldsymbol{x}_1, \boldsymbol{x}_2; t) = \langle c(\boldsymbol{x}_1, t) c(\boldsymbol{x}_2, t)\rangle$. This offers the possibility of an intuitive interpretation of the energy cascade phenomenology and gives insights into measurable statistical objects such as the scalar spectrum $E_c(k)$, which is the Fourier transform of $\mathcal{C}_2^c$. From (9) and averaging over f_c and $\boldsymbol{v}$, we obtain

$$\mathcal{C}_2^c(\boldsymbol{x}_1, \boldsymbol{x}_2; t) = \left\langle \int_0^t \mathrm{d}s_1 \int_0^t \mathrm{d}s_2 \langle f_c(\boldsymbol{\rho}(s_1; \boldsymbol{x}_1, t)) f_c(\boldsymbol{\rho}(s_2; \boldsymbol{x}_2, t))\rangle_f \right\rangle_{\boldsymbol{wv}}. \tag{13}$$

Introducing the velocity-averaged two-particle propagator $\langle P_2(\boldsymbol{y}_1, \boldsymbol{y}_2, s|\boldsymbol{x}_1, \boldsymbol{x}_2, t)\rangle_v$, which evolves according to the straightforward generalization of (10, 11) to two particles, and using (5), equation (13) reduces to

$$\mathcal{C}_2^c(\boldsymbol{x}_1, \boldsymbol{x}_2; t) = \int_0^t \mathrm{d}s \iint \langle P_2(\boldsymbol{y}_1, \boldsymbol{y}_2, s|\boldsymbol{x}_1, \boldsymbol{x}_2, t)\rangle_v \mathcal{F}(|\boldsymbol{y}_1 - \boldsymbol{y}_2|/\ell_f)\, \mathrm{d}\boldsymbol{y}_1\, \mathrm{d}\boldsymbol{y}_2, \tag{14}$$

which has a clear physical interpretation. Since $\mathcal{F}(x)$ is vanishingly small for $x \gg 1$, the correlation $\mathcal{C}_2^c$ is essentially the average time spent by a particle pair with a separation $r = |\boldsymbol{x}_1 - \boldsymbol{x}_2|$ below the forcing scale ℓ_f. Owing to the explosive separation of particles, this time has a finite limit for $r \to 0$, which yields the leading contribution to $\mathcal{C}_2^c$. The subleading behaviour is uncovered by the second-order structure function

$$S_2^c(r) = \langle (c(\boldsymbol{x}_1, t) - c(\boldsymbol{x}_2, t))^2\rangle = 2(\mathcal{C}_2^c(0) - \mathcal{C}_2^c(r)), \tag{15}$$

which is approximately the average time $\mathcal{T}_{\ell_f}(r)$ taken by two coinciding particles to reach a separation r. For a Kolmogorov's 1941 turbulent flow ($h = 1/3$), one has $S_2^c(r) \sim r^{2/3}$, i.e. $E_c(k) \sim k^{-5/3}$, which is the Oboukov–Corrsin dimensional expectation [4].

The Lagrangian description can be extended also to higher-order statistics as multipoint correlation functions $C_N^c(\boldsymbol{x}_1, \ldots, \boldsymbol{x}_N) = \langle c(\boldsymbol{x}_1, t) \ldots c(\boldsymbol{x}_N, t)\rangle$. However, when many points come into play, their geometrical arrangement becomes crucial. Dimensional arguments, which are based on the size of the configuration but forcibly neglect the 'angular' information, fall short of capturing the observed behaviour for multipoint observables. A detailed discussion of their properties is beyond the scope of this brief review. In the following, we just summarize the main concepts, referring to [25, 29] for further reading.

Expanding the power in the definition of the structure functions $S_N^c(r)$, it is necessary to express them as a linear combination of N-point correlation functions (see e.g. (15) for $S_2^c(r)$). Therefore, the latter must contain a contribution, denoted as $\mathcal{Z}_N^c(\boldsymbol{x}_1, \ldots, \boldsymbol{x}_N)$, which carries the anomalous scale dependence: $\mathcal{Z}_N^c(\lambda\boldsymbol{x}_1, \ldots, \lambda\boldsymbol{x}_N) = \lambda^{\zeta_N^c}\mathcal{Z}_N^c(\boldsymbol{x}_1, \ldots, \boldsymbol{x}_N)$ [22]–[24]. From a Lagrangian viewpoint, the function $\mathcal{Z}_N^c$ has a special property that distinguishes it from a generic scaling function. A remarkable finding is that [26, 29]

$$\frac{\mathrm{d}}{\mathrm{d}t}\langle \mathcal{Z}_N^c \rangle_{\mathcal{L}} = 0, \tag{16}$$

where the derivative $\mathrm{d}/\mathrm{d}t$ is taken along the trajectories of N particles advected by the flow and the average is over the ensemble of all trajectories. In other terms, $\mathcal{Z}_N^c$ is *statistically preserved* by the flow [26, 30]. The universality of scaling exponents is then just a by-product of the definition of statistically preserved structures: since f_c does not appear in equation (16), the properties of zero modes are insensitive to the choice of the forcing.

2.3. Dissipative anomaly

In spite of the continuous injection of scalar through the pumping f_c, the second-order moment $\langle c^2(\boldsymbol{x}, t)\rangle$ does not grow indefinitely even in the limit $\kappa \to 0$. This is due to the existence of a finite non-zero limit of the scalar dissipation $\epsilon_c = \kappa|\nabla c|^2$, which is the dissipative anomaly.

To understand how $\langle c^2(\boldsymbol{x}, t)\rangle$ achieves a finite value independent of the diffusivity coefficient, we adopt the Lagrangian viewpoint. From equation (13), we have

$$\langle c^2(\boldsymbol{x}, t)\rangle = \left\langle \int_0^t \int_0^t \mathrm{d}s_1\, \mathrm{d}s_2\, f_c(\boldsymbol{\rho}(s_1; \boldsymbol{x}, t))\, f_c(\boldsymbol{\rho}(s_2; \boldsymbol{x}, t)) \right\rangle = \left\langle \left(\int_0^t \mathrm{d}s f_c(\boldsymbol{\rho}(s; \boldsymbol{x}, t)) \right)^2 \right\rangle, \tag{17}$$

where the brackets indicate the average over the scalar forcing, the velocity field and the noise.

Looking naively at equation (17), one might expect that for a large class of random forcing of zero mean, the r.h.s. of the above expression would grow linearly with t. For instance, when the forcing is Gaussian and δ-correlated in time, one could argue that equation (17) is essentially the sum of independent variables and, by central limit theorem arguments, conclude that $\langle c^2\rangle \propto t$. This conclusion would be correct if, in the limit $\kappa \to 0$, all trajectories collapse onto a unique Lagrangian path. This turns out to be the case for strongly compressible flows, but not in general. For compressible flows, energy indeed grows linearly in time and the advected scalar performs an inverse cascade process [31, 32]. In contrast, in rough incompressible flows, coinciding particles typically separate in a finite time, giving rise to multiple paths. As a consequence, a self-averaging

process takes place in (17) and this prevents the indefinite growth of the energy. This is evident when (17) is rewritten as

$$\langle c^2(\boldsymbol{x},t)\rangle = \int_0^t \mathrm{d}s \iint \langle P_2(\boldsymbol{y}_1,\boldsymbol{y}_2,s|\boldsymbol{x},\boldsymbol{x},t)\rangle_v \mathcal{F}(|\boldsymbol{y}_1-\boldsymbol{y}_2|/\ell_f)\,\mathrm{d}\boldsymbol{y}_1\,\mathrm{d}\boldsymbol{y}_2. \tag{18}$$

The time integral is cut off at $|t-s| \gg \mathcal{T}_{\ell_f}$, which is four times larger than the (finite) time needed by two coinciding particles to separate by a distance larger than the forcing correlation length ℓ_f. This is the mechanism leading to finite dissipation of energy. To summarize, the incompressibility and roughness of the flow result in the dissipative anomaly by explosive separation of the particle paths. Further discussion on the role of dissipative anomaly in passive scalar turbulence can be found in [21, 31, 33].

3. 2D turbulent convection

An interesting problem in the context of turbulent transport is the advection of inhomogeneous temperature fields in a gravitational field. Temperature fluctuations induce density fluctuations, which in turn, via buoyancy forces, affect the velocity field: hence, the temperature field is an active scalar [4, 5]. In this paper, we consider 2D convection, which is also of experimental interest in Hele–Shaw flows [34]. As an additional asset, the 2D problem is better suited for the study of scaling properties, since it allows us to achieve higher resolution and larger statistics.

2D convection is described by the following equations:

$$\partial_t a + \boldsymbol{v}\cdot\boldsymbol{\nabla} a = \kappa\Delta a + f_a, \tag{19}$$

$$\partial_t \boldsymbol{v} + \boldsymbol{v}\cdot\boldsymbol{\nabla}\boldsymbol{v} = -\boldsymbol{\nabla} p + \nu\Delta\boldsymbol{v} - \beta a\boldsymbol{g} - \alpha\boldsymbol{v}, \tag{20}$$

where a is the field of temperature fluctuations. The second equation is the 2D Navier–Stokes equation, where $\boldsymbol{v}$ is forced by the buoyancy term $-\beta\boldsymbol{g}a$ in the Boussinesq approximation [4]; $\boldsymbol{g} = g\hat{\boldsymbol{y}}$ is acceleration due to gravity and β the thermal expansion coefficient. Kinetic energy is removed at the large scales by the friction term $-\alpha\boldsymbol{v}$. The friction is physically due to the drag experienced by a thin (quasi-$2d$) layer of fluid with the walls or air [7, 35]; α is related to the thickness of the fluid layer. A passive scalar c, evolving according to equation (2) in the same flow, has been considered as well for comparison.

Before looking at the active/passive scalar issue, let us briefly recall the phenomenology of 2D turbulent convection (for the 3D case, see e.g. [4, 5]). The balance of buoyancy and inertial terms in equation (20) introduces the Bolgiano length scale ℓ_B [4]. At small scales $r \ll \ell_B$, the inertial term is larger than buoyancy forces and the temperature is basically a passive scalar. At large scales $r \gg \ell_B$, buoyancy dominates and affects the velocity, which performs an inverse energy cascade in two dimensions. However, at variance with the usual 2D Navier–Stokes turbulence, the kinetic energy input rate ε depends here on the scale. Dimensional arguments yield $\varepsilon(r) = \beta\boldsymbol{g}\cdot\langle\boldsymbol{v}(\boldsymbol{x}+\boldsymbol{r},t)a(\boldsymbol{x},t)\rangle \sim r^{4/5}$, the Bolgiano scaling for the velocity structure functions

$$S_N^v(r) \sim (\varepsilon(r)r)^{N/3} \sim r^{\zeta_N^v}, \qquad \zeta_N^v = 3N/5, \tag{21}$$

and for temperature

$$S_N^a(r) \sim r^{\zeta_N^a}, \qquad \zeta_N^a = N/5. \tag{22}$$

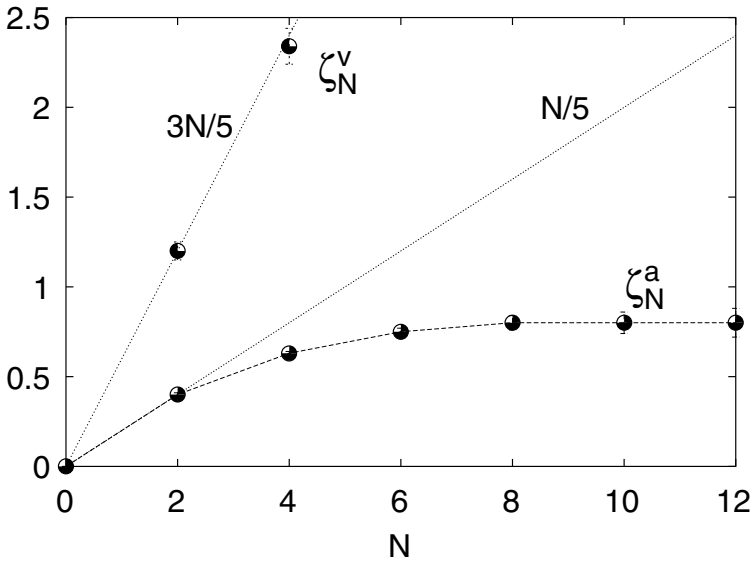

Figure 1. Scaling exponents of temperature, ζ_N^a, and velocity, ζ_N^v. The straight lines are the dimensional predictions: $N/5$ for temperature and $3N/5$ for velocity. Details of the numerics may be found in [11]. Notice that at orders larger than $N = 8$, the temperature exponents saturate to a constant value, $\zeta_\infty^a \simeq 0.8$.

No intermittency corrections are reported for the velocity, whereas the temperature field is strongly intermittent (see figure 1 and [11, 36]).

Summarizing, the temperature fluctuations are injected at scales $\sim \ell_f$, pump kinetic energy through the buoyancy term and a non-intermittent velocity inverse cascade is established with $\delta_r v \sim r^{3/5}$. The presence of friction stabilizes the system, inducing a statistically steady state. The active and passive scalars are, therefore, transported by a self-similar, incompressible and rough flow. An intermittent cascade of fluctuations with anomalous, universal scaling exponents ζ_N^c is observed for the passive scalar.

Our aim is to compare the statistical properties of the temperature field and the passive scalar field. For this purpose, in [11], equations (19) and (20) were integrated with f_a and f_c, chosen as two independent realizations of a stochastic, isotropic, homogeneous and Gaussian process of zero mean and correlation

$$\langle f_i(\boldsymbol{x}, t) f_j(\boldsymbol{x}', t') \rangle = \delta_{ij} \delta(t - t') \mathcal{F}(|\boldsymbol{x} - \boldsymbol{x}'|/\ell_f), \tag{23}$$

where $\mathcal{F}(r/\ell_f) = \exp(-r^2/(2\ell_f^2))$ decreases rapidly as $r \geqslant \ell_f$. The labels are $i, j = a, c$. Results of this numerical study clearly confirm that scaling exponents of temperature are anomalous (figure 1), and coincide with those of the passive field $\zeta_N^c = \zeta_N^a$ (figure 2, left panel).

In this system, there is saturation of intermittency, i.e. for large N, the scaling exponents saturate to a constant $\zeta_\infty^{a,c} \approx 0.8$ (see figure 1). This phenomenon, well known for passive scalars [19], is physically related to the presence of abrupt changes in the spatial structure of the scalar field ('fronts'). In the temperature field, these quasi-discontinuities correspond to the boundaries between hot rising and cold descending patches of fluid [36]. It is worth mentioning that saturation has been experimentally observed both for passive scalars [37, 38] and temperature fields [39].

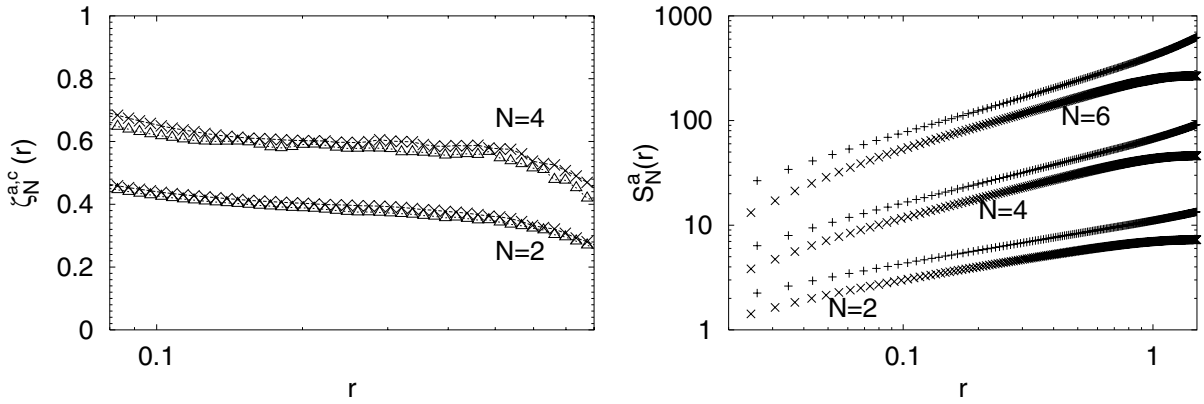

Figure 2. Left: local scaling exponents of temperature (×) and concentration (△) fluctuations, $\zeta_N^{a,c}(r) = \mathrm{d}\ln S_N^{a,c}(r)/\mathrm{d}\ln r$. Temperature and concentration are driven by independent Gaussian random forcing with correlation function as equation (23). Right: temperature structure functions $S_N^a(r)$ for $N = 2, 4, 6$ as a function of the separation r. The two sets of curves were generated by using the random (×) and mean gradient (+) forcings. Notice that the curves are parallel within the inertial range. The curves have been enlarged for clarity.

Clear evidences of saturation have recently been obtained also in the convective atmospheric boundary layer exploiting the large-eddy simulation technique [40].

These findings point to the conclusion that the temperature and the passive scalar have the same scaling laws. It remains to be ascertained whether the temperature scaling exponents are universal with respect to the forcing. To this end, a set of simulations were performed in [11, 36], with a forcing that mimics the effect of a superimposed mean gradient on the transported temperature field

$$f_a(\boldsymbol{x}, t) = \gamma \boldsymbol{g} \cdot \boldsymbol{v}(\boldsymbol{x}, t). \tag{24}$$

Remarkably, the results show that the scaling exponents of the temperature field do not depend on the injection mechanism (figure 2, right panel), suggesting universality [11, 36]. Another outcome of this investigation is that the velocity field statistics itself is universal with respect to the injection mechanism of the temperature field. Indeed, $\boldsymbol{v}$ displays a close-to-Gaussian and non-intermittent statistics with both forcings (23) and (24) [11]. This is most probably a consequence of the observed universal Gaussian behaviour of the inverse energy cascade in 2D Navier–Stokes turbulence [41, 42]. Indeed, velocity fluctuations in 2D convection also arise from an inverse cascade process driven by buoyancy forces.

So far, all the numerical evidences converge to the following global picture of scaling and universality in 2D turbulent convection. Velocity statistics is strongly universal with respect to the temperature-external driving f_a. Temperature statistics shows anomalous scaling exponents that are universal and coincide with those of a passive scalar evolving in the same flow. It is noteworthy that similar findings have been obtained in the context of simplified shell models for turbulent convection [14, 15].

The observed universality of the temperature-scaling exponents suggests that a mechanism similar to that of passive scalars may be at work, i.e. that statistically preserved structures may

also exist for the (active) temperature. Pursuing this line of thought, one may be tempted to define them through the property $(\mathrm{d}/\mathrm{d}t)\langle \mathcal{Z}_N^a \rangle_{\mathcal{L}} = 0$ as for passive scalars (see equation (16)). However, statistically preserved structures are determined by the statistics of particle trajectories, which, through the feedback of a on $\boldsymbol{v}$, depend on f_a. Therefore, the above definition does not automatically imply the universality of $\mathcal{Z}_N^a$, because Lagrangian paths depend on f_a. Nonetheless, the observed universality of the statistics of $\boldsymbol{v}$ is sufficient to guarantee universality of the trajectories statistics, leading to the conclusion that if $\mathcal{Z}_N^a$ exists, it might be universal. Since $\mathcal{Z}_N^c$ are also defined by the Lagrangian statistics, which is the same for a and c, we may further conjecture that $\mathcal{Z}_N^a = \mathcal{Z}_N^c$. This would explain the equality of scaling exponents, $\zeta_N^a = \zeta_N^c$.

It has to be remarked that this picture is probably not generic. Two crucial points are needed to have the equality between active and passive scalar exponents: (*i*) the velocity statistics should be universal; and (*ii*) the correlation between f_a and the particle paths should be negligible. As we shall see in the following, those two requirements are not generally met.

4. 2D MHD

4.1. Direct and inverse cascades

MHD models are extensively used in the study of magnetic fusion devices, industrial processing plasmas and ionospheric/astrophysical plasmas [3]. MHD is the extension of hydrodynamics to conductive fluids, including the effects of electromagnetic fields. When the magnetic field $\boldsymbol{b}$ has a strong large-scale component in one direction, the dynamics is adequately described by the 2D MHD equations [6]. Since the magnetic field $\boldsymbol{b}(\boldsymbol{x}, t)$ is solenoidal, in $2d$, it can be represented in terms of the magnetic scalar potential $a(\boldsymbol{x}, t)$, i.e. $\boldsymbol{b} = -\boldsymbol{\nabla}^{\perp} a = (-\partial_2 a, \partial_1 a)$. The magnetic potential evolves according to the advection–diffusion equation

$$\partial_t a + \boldsymbol{v} \cdot \boldsymbol{\nabla} a = \kappa \Delta a + f_a, \tag{25}$$

and will be our active scalar throughout this section. The advecting velocity field is driven by the Lorentz force $(\boldsymbol{\nabla} \times \boldsymbol{b}) \times \boldsymbol{b} = -\Delta a \boldsymbol{\nabla} a$, so that the Navier–Stokes equation becomes

$$\partial_t \boldsymbol{v} + \boldsymbol{v} \cdot \boldsymbol{\nabla} \boldsymbol{v} = -\boldsymbol{\nabla} p + \nu \Delta \boldsymbol{v} - \Delta a \boldsymbol{\nabla} a. \tag{26}$$

The question is whether the picture drawn for the temperature field in $2d$ convection applies to the magnetic potential as well.

Equations (25) and (26) have two quadratic invariants in the inviscid and unforced limit, namely the total energy $\frac{1}{2}\int (v^2 + b^2)\,\mathrm{d}\boldsymbol{x}$ and the mean square magnetic potential $\frac{1}{2}\int a^2\,\mathrm{d}\boldsymbol{x}$. Using standard quasi-equilibrium arguments [6], an inverse cascade of the magnetic potential is expected to take place in the forced and dissipated case [43]. This expectation has been confirmed in numerical experiments [44]. Let us now compare the magnetic potential with a passive scalar evolving in the same flow.

We performed a high-resolution (4096^2 collocation points) direct numerical simulation of equations (25) and (26) along with a passive scalar (2). The scalar forcing terms f_a and f_c are homogeneous, independent Gaussian processes with zero mean and correlation

$$\langle \hat{f}_i(\boldsymbol{k}, t)\, \hat{f}_j(\boldsymbol{k}', t') \rangle = \frac{F_0}{(2\pi k_f)} \delta_{ij} \delta(\boldsymbol{k} + \boldsymbol{k}') \delta(k - k_f) \delta(t - t'), \tag{27}$$

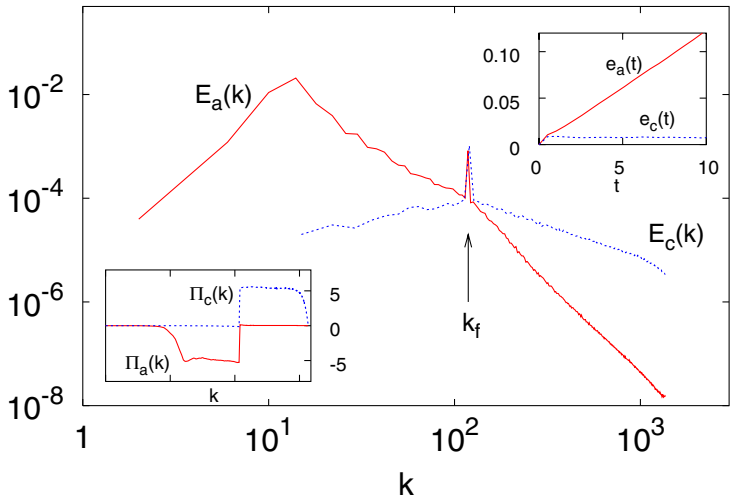

Figure 3. Power spectra of the active (red) and passive (blue) scalar variances, $E_a(k) = \pi k|\hat{a}(\boldsymbol{k}, t)|^2$ and $E_c(k) = \pi k|\hat{c}(\boldsymbol{k}, t)|^2$. Inset (below): the fluxes of scalar variance $\Pi_{a,c}$ out of wavenumber k. Negative values indicate an inverse cascade. Inset (above): the total scalar variance $e_{a,c}(t) = \int E_{a,c}(k, t)\,\mathrm{d}k$. The active variance $e_a(t)$ grows linearly in time, whereas $e_c(t)$ fluctuates around a finite value (see text). The rate of active to passive scalar dissipation is $\epsilon_a/\epsilon_c \simeq 0.005$. All fields are set to zero at $t = 0$, and time, is defined in units of eddy-turnover time $\mathcal{T} = l_f/v_{\mathrm{rms}}$, where $l_f = 2\pi/k_f$. At $k < k_f$, we observe power-law behaviours $E_a(k) \sim k^{-2.0\pm0.1}$ and $E_c(k) \sim k^{0.7\pm0.1}$, whereas at $k > k_f$, we find $E_a(k) \sim k^{-3.6\pm0.1}$ and $E_c(k) \sim k^{-1.4\pm0.1}$.

where $i, j = a, c$. The injection length scale $l_f \sim 2\pi/k_f$ has been chosen roughly in the middle of the available range of scales. F_0 is the rate of scalar variance input.

In figure 3, we summarize the spectral properties of the two scalars. The emerging picture is as follows. While a undergoes an inverse cascade process, c cascades down-scale. This striking difference is reflected in the behaviour of the dissipation. The active scalar dissipation $\epsilon_a = \kappa|\nabla a|^2$ vanishes in the limit $\kappa \to 0$, being not a dissipative anomaly for the field a. Consequently, the squared magnetic potential grows linearly in time $e_a(t) = \frac{1}{2}\int a^2\,\mathrm{d}\boldsymbol{x} \approx \frac{1}{2}F_0 t$. On the contrary, for the passive scalar, a dissipative anomaly is present and $\epsilon_c = \kappa|\nabla c|^2$ equals the input $\frac{1}{2}F_0$ holding c in a statistically stationary state (see inset to figure 3).

The velocity field is rough (as confirmed by its spectrum, see figure 4) and incompressible; therefore particle paths are not unique and explosively separate. This entails the dissipative anomaly for passive scalars. In contrast, the dissipative anomaly is absent from the magnetic potential despite the fact that the trajectories are the same—the advecting velocity is the same. How can these two seemingly contradictory statements be reconciled?

4.2. Dissipative anomaly and particle paths

The solution of the riddle resides in the relationship between the Lagrangian trajectories and the active scalar input f_a. These two quantities are bridged by the Lorentz force appearing in (26). To study the correlations between forcing and particle paths, we need to compute

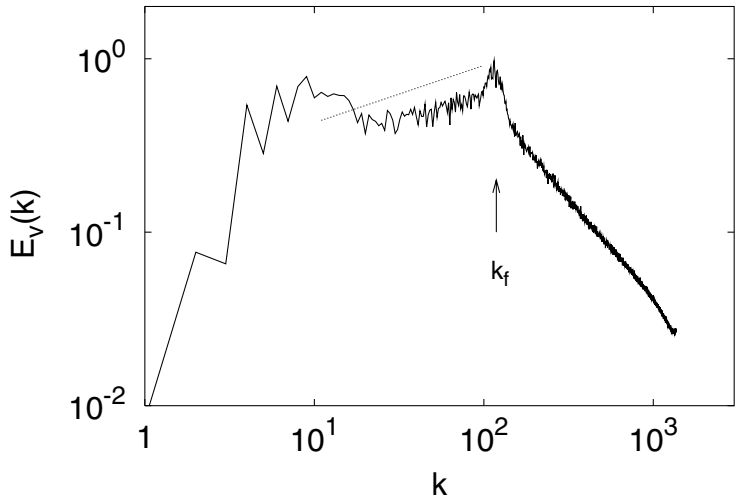

Figure 4. Velocity power spectrum $E_v(k) = \pi k|\hat{v}(\boldsymbol{k}, t)|^2$. For $k < k_f$, in agreement with previous simulations [44], we observe $E_v(k) \sim k^{1/3}$ $(\cdot\ \cdot\ \cdot)$, which deviates from the dimensional prediction $k^{-1/3}$. In the range $k > k_f$, a scaling close to $k^{-5/3}$ is observed, indicating that $\boldsymbol{v}$ is rough both in the inverse and direct cascade ranges.

the evolution of the particle propagator. The relevant observables are the time sequences of $\phi_{a,c}(s) = \int \mathrm{d}\boldsymbol{y}\, f_{a,c}(\boldsymbol{y}, s) P(\boldsymbol{y}, s|\boldsymbol{x}, t)$. Indeed, the equivalent of equation (12) can be written for the active scalar as

$$a(\boldsymbol{x}, t) = \int_0^t \mathrm{d}s \int \mathrm{d}\boldsymbol{y}\, f_a(\boldsymbol{y}, s) P(\boldsymbol{y}, s|\boldsymbol{x}, t). \tag{28}$$

The main difficulty encountered here is that P evolves *backward* in time according to (10) and the condition $P(\boldsymbol{y}, t|\boldsymbol{x}, t) = \delta(\boldsymbol{y} - \boldsymbol{x})$ is set at the final time t. Conversely, the initial conditions on velocity and scalar fields are set at the initial time. The solution of this mixed initial/final value problem is a nontrivial numerical task. To this end, we devised a fast and low-memory demanding algorithm to integrate equations (25), (26) and (10) with the appropriate initial/final conditions. Details are given in [45].

The typical evolution of the propagator is shown in the middle column of figure 5. From its evolution, we reconstructed the time sequences of the forcing contributions $\phi_{a,c}(s)$, which, when, integrated over s, yield the amplitude of the scalar fields according to equations (12) and (28). The time series of $\phi_a(s)$ and $\phi_c(s)$ are markedly different (figure 6), the former being strongly skewed towards positive values at all times. This signals that trajectories preferentially select regions where f_a has a positive sign, summing up forcing contributions to generate a typical variance of a of the order $F_0 t$. On the contrary, the passive scalar sequence displays the usual features: f_c is independent of P and their product can be positive or negative with equal probability on distant trajectories. This ensures that the time integral in equation (12) averages out to zero for $|s - t| > \mathcal{T}_{\ell_f}$ (see section 2.2) and yields $c^2 \sim F_0 \mathcal{T}_{\ell_f}$.

As shown in figure 6 (lower panel), the effect of correlations between the forcing and propagator is even more striking comparing $\int_0^s \mathrm{d}s' \phi_a(s')$ with $\int_0^s \mathrm{d}s' \phi_c(s')$. The conspicuous

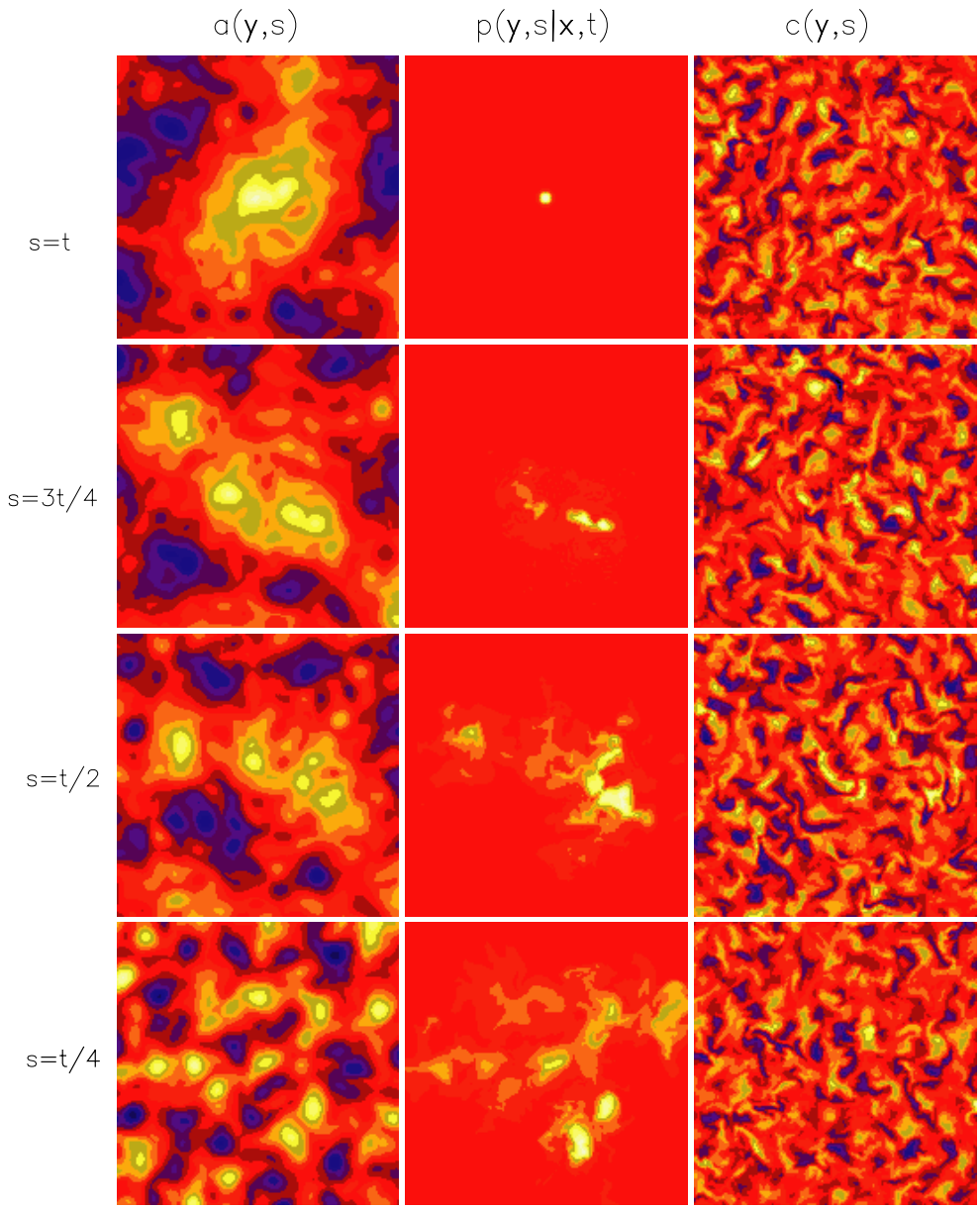

Figure 5. Time runs from bottom to top. First column: time evolution of the active scalar field resulting from the numerical integration of equations (25) and (26). Second column: backward evolution of the particle propagator according to equation (10). Third column: time evolution of the passive scalar field in the same flow.

difference is related to a strong spatial correlation between P and a, as can be inferred from

$$\int_0^s \phi_a(s')\,\mathrm{d}s' = \int \mathrm{d}\boldsymbol{y}\, a(\boldsymbol{y}, s)\, P(\boldsymbol{y}, s|\boldsymbol{x}, t), \tag{29}$$

which can be derived from (25) and (11). An equivalent relation holds for c as well. Comparison of the first and second columns of figure 5 highlights the role of spatial correlations: the distribution

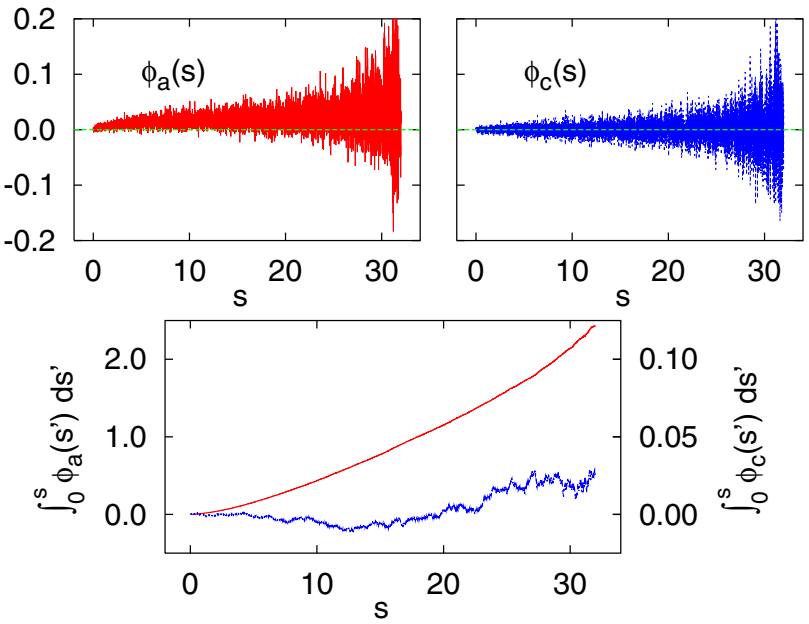

Figure 6. Top panel: $\phi_{a,c}(s) = \int \mathrm{d}\boldsymbol{y}\, f_{a,c}(\boldsymbol{y}, s) P(\boldsymbol{y}, s|\boldsymbol{x}, t)$. The two graphs have the same scale on the vertical axis. Here, $t = 32$. Bottom panel: time integrals $\int_0^s \phi_a(s')\,\mathrm{d}s'$ (upper curve) and $\int_0^s \phi_c(s')\,\mathrm{d}s'$ (lower curve). Note the different scale on the vertical axis. Recall that $\int_0^t \phi_a(s')\,\mathrm{d}s' = a(\boldsymbol{x}, t)$ (and similarly for c).

of particles follows the distribution of the active scalar. This amounts to saying that large-scale scalar structures are built out of smaller ones that coalesce together [44]. This has to be contrasted with the absence of large-scale correlations between the propagator and the passive scalar field (figure 5, columns 2 and 3).

Let us now clarify the mechanism for the absence of dissipative anomaly. Consider the squared active field a^2. It can be expressed in two equivalent ways. On the one hand, it can be written as the square of (28). On the other, by multiplying equation (25) by $2a$, one obtains the equation

$$\partial_t a^2 + \boldsymbol{v} \cdot \nabla a^2 = \kappa \Delta a^2 + 2a f_a - 2\epsilon_a. \tag{30}$$

Exploiting the absence of dissipative anomaly $\epsilon_a = 0$, equation (30) reduces to a transport equation that can be solved in terms of particle trajectories. Comparison of the two expressions yields[6]

$$\begin{aligned}&\int_0^t \mathrm{d}s \int_0^t \mathrm{d}s' \iint f_a(\boldsymbol{y}, s) f_a(\boldsymbol{y}', s') P(\boldsymbol{y}, s|\boldsymbol{x}, t) P(\boldsymbol{y}', s'|\boldsymbol{x}, t)\\ &= \int_0^t \mathrm{d}s \int_0^t \mathrm{d}s' \iint f_a(\boldsymbol{y}, s) f_a(\boldsymbol{y}', s') P(\boldsymbol{y}', s'; \boldsymbol{y}, s|\boldsymbol{x}, t),\end{aligned} \tag{31}$$

[6] To obtain the r.h.s. of (31), consider the expression $a^2(\boldsymbol{x}, t) = 2\int_0^t \mathrm{d}s \int \mathrm{d}\boldsymbol{y}\, f_a(\boldsymbol{y}, s) a(\boldsymbol{y}, s)$, insert $a(\boldsymbol{y}, s) = \int_0^s \mathrm{d}s' \int \mathrm{d}\boldsymbol{y}'\, f_a(\boldsymbol{y}', s')$, i.e. equation (4) evaluated at time s, and exploit the symmetry under exchange of s and s' to switch from a time-ordered form to a time-symmetric one to get rid of the factor 2.

where $P(\boldsymbol{y}', s'; \boldsymbol{y}, s|\boldsymbol{x}, t) = P(\boldsymbol{y}, s|\boldsymbol{x}, t)\,P(\boldsymbol{y}', s'|\boldsymbol{y}, s)$ denotes the probability that a trajectory ending in $(\boldsymbol{x}, t)$ is in $(\boldsymbol{y}, s)$ and $(\boldsymbol{y}', s')$. Integration over $\boldsymbol{y}$ and $\boldsymbol{y}'$ is implied. Equation (31) amounts to saying that

$$\left\langle \int_0^t f_a(\boldsymbol{\rho}(s), s)\,\mathrm{d}s \right\rangle_{\boldsymbol{w}}^2 = \left\langle \left[\int_0^t f_a(\boldsymbol{\rho}(s), s)\,\mathrm{d}s \right]^2 \right\rangle_{\boldsymbol{w}}, \tag{32}$$

meaning that $\int_0^t f_a(\boldsymbol{\rho}(s), s)\,\mathrm{d}s$ is a *non-random* variable over the ensemble of trajectories. The above procedure can be generalized to show that $\langle \int_0^t f_a(\boldsymbol{\rho}(s), s)\,\mathrm{d}s\rangle_{\boldsymbol{w}}^N = \langle [\int_0^t f_a(\boldsymbol{\rho}(s), s)\,\mathrm{d}s]^N\rangle_{\boldsymbol{w}}$.

In plain words, the absence of the dissipative anomaly is equivalent to the property that, along any of the infinite trajectories $\boldsymbol{\rho}(s)$ ending in $(\boldsymbol{x}, t)$, the quantity $\int_0^t f_a(\boldsymbol{\rho}(s), s)\,\mathrm{d}s$ is exactly the same, and equals $a(\boldsymbol{x}, t)$. Therefore, a single trajectory suffices to obtain the value of $a(\boldsymbol{x}, t)$, contrary to the passive case where different trajectories contribute disparate values of $\int_0^t f_c(\boldsymbol{\rho}(s), s)\,\mathrm{d}s$, with a typical spread $\epsilon_c t$, and only the average over all trajectories yields the correct value of $c(\boldsymbol{x}, t)$. In the unforced case, particles move along isoscalar lines: this is how non-uniqueness and explosive separation of trajectories are reconciled with the absence of dissipative anomaly.

Inverse cascades appear also for passive scalars in compressible flows [32]. There, the ensemble of the trajectories collapses onto a unique path, fulfilling in the simplest way the constraint (31). In MHD, the constraint is satisfied owing to a subtle correlation between the forcing and trajectories peculiar to the active case.

MHD in two dimensions represents an 'extreme' example of the effect of correlations among Lagrangian paths and the active scalar input. The property that all trajectories ending in the same point should contribute the same value of the input poses a global constraint over the possible paths.

Before discussing the statistical properties of a, on the basis of the previous discussion, it is instructive to reconsider the concept of dissipative anomaly in general scalar turbulence.

4.3. Dissipative anomaly revisited

In this subsection, we give an alternative interpretation of dissipative anomaly. To this aim, let us denote by $\Theta(\boldsymbol{x}, t)$ a generic scalar field, regardless of its passive or active character. The scalar evolves according to the transport equation

$$\partial_t \Theta + \boldsymbol{v}\cdot\nabla\Theta = \kappa\Delta\Theta + f_\Theta. \tag{33}$$

We can formally solve equation (33) by the method of characteristics, i.e. in terms of the stochastic ordinary differential equations

$$\frac{\mathrm{d}\boldsymbol{\rho}(t)}{\mathrm{d}t} = \boldsymbol{v}(\boldsymbol{\rho}(t), t) + \sqrt{2\kappa}\dot{\boldsymbol{w}}, \tag{34}$$

$$\frac{\mathrm{d}\vartheta(t)}{\mathrm{d}t} = f_\Theta(\boldsymbol{\rho}(t), t). \tag{35}$$

Here, we are not conditioning *a priori* the paths to their final positions in contrast with the procedure adopted in section 2.2. The Eulerian value of the field is recovered once the average

over all paths $\boldsymbol{\rho}$ landing in $(\boldsymbol{x}, t)$ is performed, i.e. $\Theta(\boldsymbol{x}, t) = \langle \vartheta(t) \rangle_{\boldsymbol{w}}$. Recall that if the flow is non-Lipschitz-continuous, such paths do not collapse onto a single one for $\kappa \to 0$ as well.

We can now define $P(\boldsymbol{x}, \vartheta, t | \boldsymbol{x}_0, \vartheta_0, 0)$ as the probability that a path that started in $\boldsymbol{x}_0$ at time 0 with $\vartheta_0 = \Theta(\boldsymbol{x}_0, 0)$ arrives in $\boldsymbol{x}$ at time t carrying a scalar value ϑ. Notice that the conditioning is now on the initial value, and P evolves according to the Kolmogorov equation

$$\partial_t P + \boldsymbol{v} \cdot \boldsymbol{\nabla}_{\boldsymbol{x}} P + f_\Theta \nabla_\vartheta P = \kappa \Delta P, \tag{36}$$

with initial condition $P(\boldsymbol{x}, \vartheta, t | \boldsymbol{x}_0, \vartheta_0, 0) = \delta(\boldsymbol{x} - \boldsymbol{x}_0)\delta(\vartheta - \vartheta_0)$ and $\vartheta_0 = \Theta(\boldsymbol{x}, 0)$.

Integrating over the initial conditions, we define now the probability density $\mathcal{P}(\boldsymbol{x}, \vartheta, t) = \int P(\boldsymbol{x}, \vartheta, t | \boldsymbol{x}_0, \Theta(\boldsymbol{x}_0, 0), 0)\, \mathrm{d}\boldsymbol{x}_0$. $\mathcal{P}$ still obeys (36) with initial condition $\mathcal{P}(\boldsymbol{x}, \vartheta, 0) = \delta(\vartheta - \Theta(\boldsymbol{x}_0, 0))$, and represents the probability that a path arrives in $(\boldsymbol{x}, t)$ carrying a scalar value $\vartheta(t) = \int_0^t f_\Theta(\rho(s), s)\, \mathrm{d}s$.

Let us now look at the variance of the distribution of such values, i.e. $\sigma^2_\Theta(\boldsymbol{x}, t) = \int \vartheta^2 \mathcal{P}\, \mathrm{d}\vartheta - (\int \vartheta \mathcal{P}\, \mathrm{d}\vartheta)^2$. From equation (36), it is easy to derive the following equation:

$$\partial_t \sigma^2_\Theta(\boldsymbol{x}, t) + \boldsymbol{v} \cdot \boldsymbol{\nabla}_{\boldsymbol{x}} \sigma^2_\Theta(\boldsymbol{x}, t) = \kappa \Delta \sigma^2_\Theta(\boldsymbol{x}, t) + 2\epsilon_\Theta(\boldsymbol{x}, t), \tag{37}$$

where $\epsilon_\Theta(\boldsymbol{x}, t) = \kappa |\boldsymbol{\nabla}_{\boldsymbol{x}} \int \vartheta \mathcal{P}(\boldsymbol{x}, \vartheta, t)\, \mathrm{d}\vartheta|^2$. In the Eulerian frame, note that $\epsilon_\Theta(\boldsymbol{x}, t) = \kappa |\boldsymbol{\nabla} \Theta(\boldsymbol{x}, t)|^2$, i.e. the local dissipation field.

Integrating over $\boldsymbol{x}$, we end up with

$$\frac{\mathrm{d}}{\mathrm{d}t} \int \sigma^2_\Theta(\boldsymbol{x}, t)\, \mathrm{d}\boldsymbol{x} = 2 \int \epsilon_\Theta(\boldsymbol{x}, t)\, \mathrm{d}\boldsymbol{x} = 2\epsilon_\Theta, \tag{38}$$

where $\epsilon_\Theta = \langle \kappa |\boldsymbol{\nabla} \Theta(\boldsymbol{x}, t)|^2 \rangle$ is the average dissipation rate of $\langle \Theta^2 \rangle / 2$. Therefore, if Θ^2 cascades towards the small scales with a finite (even in the limit $\kappa \to 0$) dissipation ϵ_Θ, the variance of the distribution of values of $\vartheta(t) = \int_0^t \mathrm{d}s\, f_\Theta(\boldsymbol{\rho}(s), s)$ will grow linearly in time. Conversely, for an inverse cascade of Θ^2 in the absence of dissipative anomaly, $\int \mathrm{d}\boldsymbol{x}\, \sigma^2_\Theta(\boldsymbol{x}, t) = 0$, corresponding to a singular distribution $\mathcal{P}(\boldsymbol{x}, \vartheta, t) = \delta(\vartheta - \Theta(\boldsymbol{x}, t))$.

In figure 7, we show the time evolution of $\int \mathrm{d}\boldsymbol{x}\, \sigma^2_{a,c}(\boldsymbol{x}, t)$ for $2d$ MHD, which confirms the above findings.

The fact that, for inverse cascading scalars, the probability density $\mathcal{P}$ collapses onto a δ-function in the limit of vanishing diffusivity amounts to saying that particles in the $(\boldsymbol{x}, \vartheta)$ space do not disperse in the ϑ-direction, but move while remaining attached to the surface $\vartheta = \Theta(\boldsymbol{x}, t)$ (see figure 8(a)). This is related to the strong spatial correlations between a and the Lagrangian propagator observed in figure 5. In contrast, for a direct cascade of scalar, such correlations do not exist and dissipation takes place because of dispersion in the ϑ-direction (see figure 8(b)).

4.4. Eulerian statistics

4.4.1. Single-point statistics. The statistical properties of the magnetic potential a and the passive scalar c are markedly different already at the level of single-point statistics. The pdf of a is Gaussian, with zero mean and variance $F_0 t$ (figure 9). Conversely, the pdf of c is stationary and super-Gaussian (see figure 9), as it generically happens for passive fields sustained by a Gaussian forcing in rough flows [25].

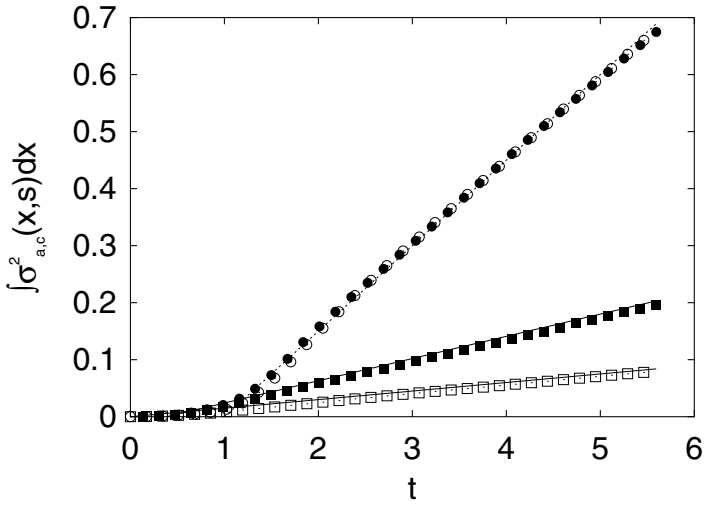

Figure 7. Plot of $\int \mathrm{d}\boldsymbol{x}\, \sigma_a^2(\boldsymbol{x}, t)$ and $\int \mathrm{d}\boldsymbol{x}\, \sigma_c^2(\boldsymbol{x}, t)$ (□ and ○ respectively) versus time. We have integrated equations (25) and (2) for two different values of diffusivity, $\kappa = 0.003$ (■ ●) at resolution 512^2 and $\kappa = 0.001$ (○ □) at resolution 1024^2. The straight lines indicate the growth laws $2\epsilon_a t$ and $2\epsilon_c t$ for the two values of κ. Note that ϵ_c does not depend on κ consistently in the presence of dissipative anomaly, whereas ϵ_a decreases as κ decreases. The variance has been evaluated averaging over 10^6 Lagrangian paths evolving according to (34). The Lagrangian scalar values ϑ_a and ϑ_c (where $a(\boldsymbol{x}, t) = \int \vartheta_a \mathcal{P}(\boldsymbol{x}, \vartheta_a, t)\, \mathrm{d}\vartheta_a$, the equivalent relation holds between c and ϑ_c) have been computed integrating (35) both for the active f_a and passive f_c forcings along each path. The forcings are chosen as in (27). The initial Eulerian $a(\boldsymbol{x}, 0), c(\boldsymbol{x}, 0)$ and Lagrangian $\vartheta_a(0), \vartheta_c(0)$ fields have been set to zero. Time is measured in eddy turnover times.

The Gaussianity of the pdf of a is a straightforward consequence of the vanishing of active scalar dissipation. This is simply derived by multiplying equation (25) for $2na^{2n-1}$ and averaging over the forcing statistics. The active scalar moments obey the equation $\partial_t \langle a^{2n} \rangle = n(2n-1) F_0 \langle a^{2n-2} \rangle$ (odd moments vanish by symmetry), whose solutions are the Gaussian moments: $\langle a^{2n} \rangle = (2n-1)!!(F_0 t)^n$. An equivalent derivation can be obtained in Lagrangian terms. Following the same steps that lead from equation (30) to (31), it is easy to derive the following expression:

$$a^{2n}(\boldsymbol{x}, t) = 2n \int_0^t \mathrm{d}s_1 \int \mathrm{d}\boldsymbol{y}_1 P(\boldsymbol{y}_1, s_1 | \boldsymbol{x}, t)\, f_\Theta(\boldsymbol{y}_1, s_1) a^{2n-1}(\boldsymbol{y}_1, s_1), \tag{39}$$

which, after integrating over $\boldsymbol{x}$ and averaging over the forcing statistics, reduces to

$$\langle a^{2n} \rangle(t) = n(2n-1) F_0 \int_0^t \mathrm{d}s \langle a^{2n-2} \rangle(s), \tag{40}$$

which, unravelling the hierarchy, yields the Gaussian moments written above. In passing from equation (39) to (40), we used the property that $\int \mathrm{d}\boldsymbol{x}\, P(\boldsymbol{y}, s | \boldsymbol{x}, t) = 1$ (which is ensured by equation (10)) and Gaussian integration by parts.

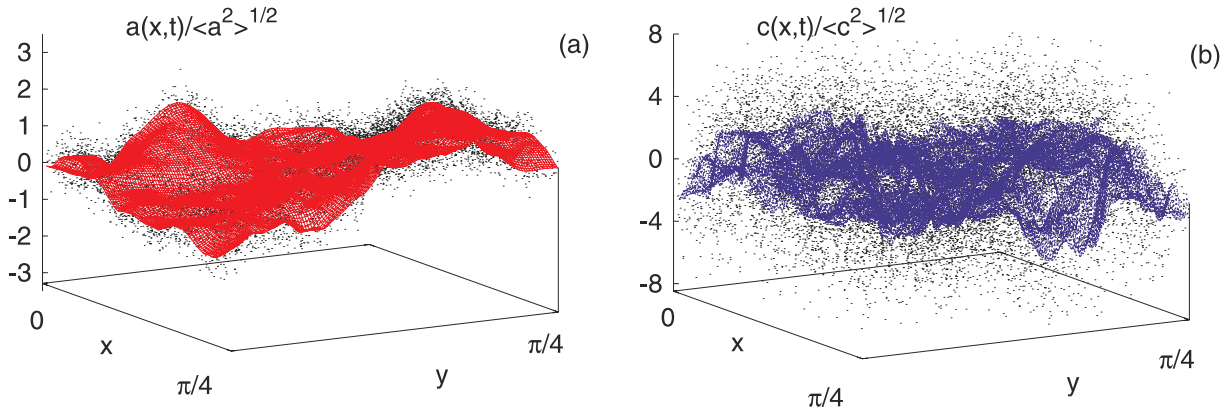

Figure 8. (a) The surface is the instantaneous Eulerian magnetic potential field $a(\boldsymbol{x}, t)$. The dots represent the positions of particles in the $(\boldsymbol{x}, \vartheta_a)$ space at time t. (b) The same for the passive scalar c. The time t corresponds to the largest time in figure 7. For visualization purposes, only the portion $[0, \pi/4] \times [0, \pi/4]$ is displayed. In (a), the cloud of dots closely follows the magnetic potential surface; however, in (b), they are considerably more dispersed (notice the difference in values of the ϑ-axis).

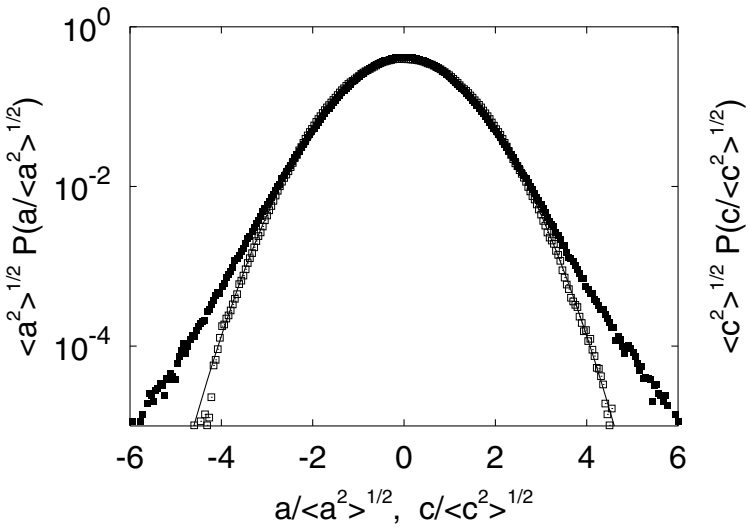

Figure 9. Pdfs of the active (□) and passive (■) scalar fields normalized by their standard deviation. The active scalar pdf is indistinguishable from a Gaussian (———).

4.4.2. Multipoint statistics and the absence of anomalous scaling in the inverse cascade. Results about two-point statistics of the magnetic potential and passive scalar fields are summarized in figure 10. In the inverse cascade scaling range $r > \ell_f$, the rescaled pdf of $\delta_r a$ at different values of the separation r collapse onto the same curve, indicating the *absence of anomalous scaling* (figure 10(a)). In contrast, in the scaling range $r < \ell_f$, the rescaled pdfs of passive scalar increments at different r values do not collapse (figure 10(b)), i.e. we have anomalous scaling, as expected.

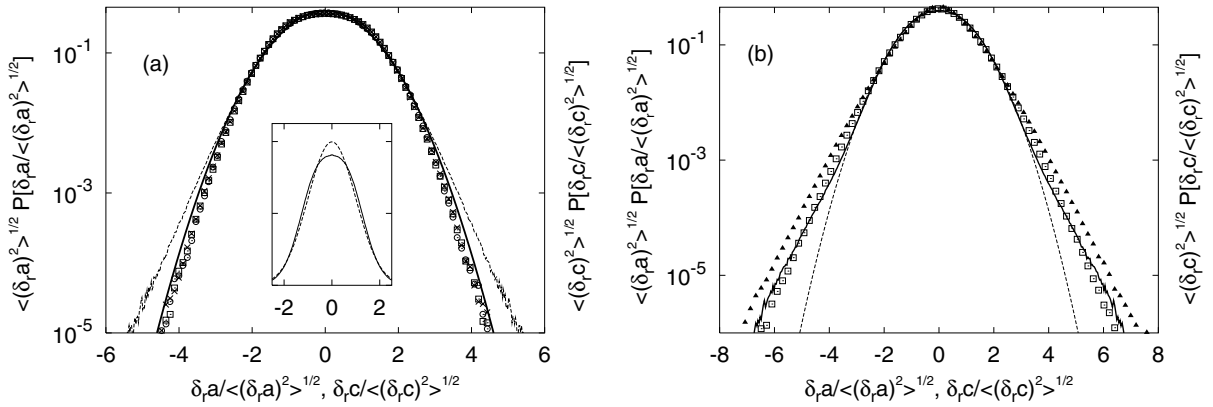

Figure 10. (a) Rescaled pdf of the normalized active scalar increments $\delta_r a/\langle(\delta_r a)^2\rangle^{1/2}$ for three separations in the $r > \ell_f$ range: $r = 2\ell_f$ (×), $3\ell_f$ (○) and $4\ell_f$ (□). Pdf of the normalized passive scalar increments at the same scales (– – –) and the Gaussian (———) are shown for comparison . In the inset, the rescaled pdf of $\delta_r a$ for $r = 3\ell_f$ (———) is shown in the interval $[-2.5 : 2.5]$ in the linear scale to emphasize the deviation from a Gaussian (– – –). The flatness is ∼2.76, significantly lower than the Gaussian value 3. (b) Rescaled pdf of the passive scalar increments $\delta_r c/\langle(\delta_r c)^2\rangle^{1/2}$ for two separations in the $r < \ell_f$ range: $r = 0.3\ell_f$ (▲) and $r = 0.6\ell_f$ (□). The rescaled pdfs of active scalar increments at the same scales (———) and a Gaussian (– – –) are reported for comparison.

Let us now consider in quantitative terms the scaling behaviours. In our simulations, the scaling range $r < \ell_f$ ($k > k_f$) was poorly resolved; therefore we do not enter the much debated issue of scaling of the magnetic and velocity fields over this range of scales (see e.g. [43, 44, 46]–[49]). Instead, we just mention that current opinions are divided between the Kolmogorov scaling $\delta_r v \sim r^{1/3}$ and the Iroshnikov–Kraichnan scaling $\delta_r v \sim r^{1/4}$, corresponding to spectral behaviours such as $E_v(k) \sim k^{-5/3}$ and $E_v(k) \sim k^{-3/2}$, respectively. Both theories agree on the smooth scaling behaviour for the magnetic potential $\delta_r a \sim r$ that is observed numerically (see figure 3). In the range of scales $r > \ell_f (k < k_f)$, standard dimensional arguments predict $E_a(k) \sim k^{-7/3}$ [6, 43, 44], which is different from our finding that $E_a(k) \sim k^{-2}$ (figure 11). In real space, this means that $\delta_r a \sim r^{1/2}$, which is dimensionally compatible with scaling behaviour $\delta_r v = [\boldsymbol{v}(\boldsymbol{x}+\boldsymbol{r}, t) - \boldsymbol{v}(\boldsymbol{x}, t)] \cdot \hat{\boldsymbol{r}} \sim r^0$ for $r > \ell_f$ (as suggested by the velocity spectrum, see figure 4), and the Yaglom relation $\langle \delta_r v (\delta_r a)^2 \rangle \simeq F_0 r$ [4]. As a side remark, note that the argument for $E_a(k) \sim k^{-7/3}$ rests on the assumption of locality for velocity increments, a hypothesis incompatible with the observed velocity spectrum at $k < k_f$ (see figure 4).

It is worth remarking that the increments of active scalar $\delta_r a = a(\boldsymbol{x}+\boldsymbol{r}, t) - a(\boldsymbol{x}, t)$ eventually reach a stationary state in spite of the growth of a^2. The distribution of $\delta_r a$ is sub-Gaussian (figure 10). This behaviour can be explained by recalling that $\delta_r a$ is the difference of two Gaussian variables, which are, however, strongly correlated (indeed the main contributions will come from $\boldsymbol{x}+\boldsymbol{r}$ and $\boldsymbol{x}$ inside the same island; see figure 5). This correlation leads to cancellations that result in the observed sub-Gaussian pdf.

Let us now focus on the most interesting aspect, namely the absence of anomalous scaling in the inverse cascade range. The absence of intermittency seems to be a common feature of inverse cascading systems as passive scalars in compressible flows [31, 32] and the velocity field

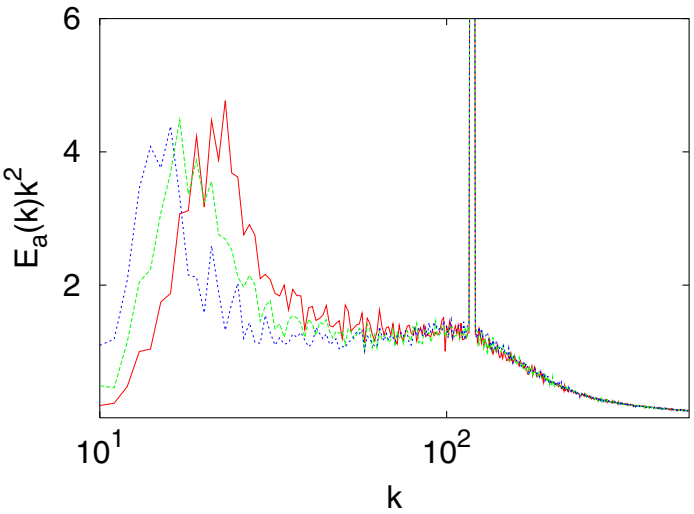

Figure 11. Compensated power spectra of active scalar variances $E_a(k)k^2$ at three different times of the evolution. Note that an increasingly clear plateau at $k < k_f$ appears.

in 2D Navier–Stokes turbulence [42]. This leads to the conjecture that an universal mechanism may be responsible for the self-similarity of inverse cascading systems. Whereas $2d$ Navier–Stokes turbulence is not fully understood, the absence of anomalous scaling from passive scalars evolving in compressible flows has been recently understood in terms of the collapse of the Lagrangian trajectories onto a unique path [31, 32]. Briefly, the collapse of trajectories allows us to express the $2N$-order structure function in terms of two-particle propagators $\langle P_2 \rangle_v$, instead of the $2N$-particle propagator $\langle P_{2N} \rangle_v$. Whereas the latter may be dominated by a zero mode with a non-trivial anomalous scaling, the former are not anomalous and lead to dimensional scaling.

The above argument cannot be simply exported to the magnetic potential inverse cascade: first, the Lagrangian paths do not collapse onto a unique one; secondly, the correlation between f_a and $\boldsymbol{v}$ does not allow us to split the averages. However, the former difficulty can be overcome. Indeed, the property that all paths landing in the same point contribute the same value has important consequences in the multipoints statistics as well. Proceeding as for the derivation of equation (31), it is possible to show that m trajectories are enough to calculate the product of arbitrary powers of a at m different points $\langle a^{n_1}(\boldsymbol{x}_1, t) \dots a^{n_m}(\boldsymbol{x}_m, t) \rangle$. In particular, structure functions $S_N^a(r) = \langle (\delta_r a)^N \rangle$ for any order N involve only two trajectories. This should be contrasted with the passive scalar, where the number of trajectories increases with N and this is at the core of anomalous scaling of passive fields [25].

5. 2D Ekman turbulence

Let us now consider the case of scalars that act on the velocity field through a functional dependence. Among them, probably the best-known case is vorticity in two dimensions $a = \nabla \times \boldsymbol{v}$. It obeys the Ekman–Navier–Stokes equation

$$\partial_t a + \boldsymbol{v} \cdot \nabla a = \kappa \Delta a - \alpha a + f_a. \tag{41}$$

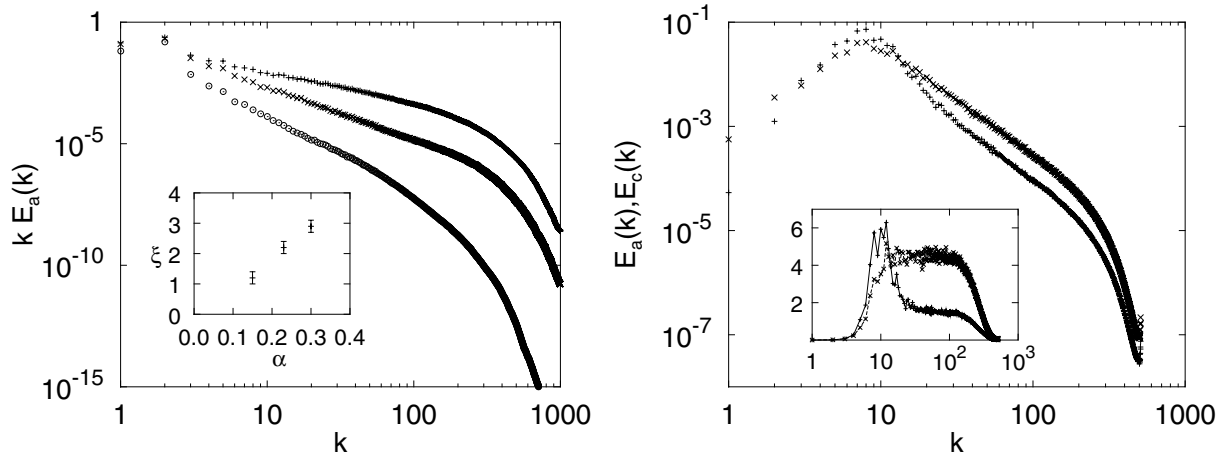

Figure 12. Left: the vorticity spectrum $E_a(k) \sim k^{-1-\xi}$ steepens by increasing the Ekman coefficient α. Here, $\alpha = 0.15$ (+), $\alpha = 0.23$ ($\times$) and $\alpha = 0.30$ ($\odot$). The inset presents the exponent ξ as a function of α. Right panel: power spectra of passive scalar ($\times$) and vorticity (+). Here, $\alpha = 0.15$. In the inset, we show the same spectra compensated by $k^{1+\zeta_2^c}$ (see [12] for details on the DNS).

The term $-\alpha\, a$ models the Ekman drag experienced by a thin fluid layer with the walls or the surrounding air [7, 35].

In the absence of friction ($\alpha = 0$), dimensional arguments [50, 51], confirmed by experiments [41, 52] and numerical simulations [42], give the following scenario. At large scales, an inverse (non-intermittent) cascade of kinetic energy takes place with $E_v(k) \sim k^{-5/3}$ and $E_a(k) \sim k^{1/3}$. At small scales, the enstrophy $\langle a^2 \rangle$ performs a forward cascade with $E_a(k) \sim k^{-1}$ and $E_v(k) \sim k^{-3}$, meaning that the velocity field is smooth over this range of scales.

In the presence of friction ($\alpha > 0$), kinetic energy is removed at large scales holding the system in a statistically steady state, and small-scale statistics is modified by the competition of the inertial ($\boldsymbol{v} \cdot \nabla a$) and friction ($-\alpha\, a$). Since these two terms have the same dimension due to smoothness of the velocity field, this results in nontrivial scaling laws for a. This effect is evident in DNS with $\alpha > 0$ [12, 17], where the vorticity spectrum displays a power law steeper than in the frictionless case: $E_a(k) \sim k^{-1-\xi}$ with ξ dependent on α (see figure 12, left panel). For $0 < \xi < 2$, the exponent ξ coincides with the scaling exponent ζ_2^a of the second-order structure function $S_2^a(r)$. Additionally, high-order structure functions at fixed α show anomalous scaling, $\zeta_N^a \neq N\xi/2$ [12]. Spectral steepening and the presence of intermittency are observed [12, 16] also in passive scalars evolving in smooth flows according to

$$\partial_t c + \boldsymbol{v} \cdot \nabla c = \kappa \Delta c - \alpha c + f_c. \tag{42}$$

Physically, equation (42) describes the evolution of a decaying passive substance (e.g. a radioactive marker) [4, 53]. For $\alpha = 0$, the dimensional expectation $E_c(k) \sim k^{-1}$ has been verified in experiments [54]. For positive α, passive scalar spectra become steeper than k^{-1} and, at high wavenumbers, have the same slope of the vorticity spectrum (figure 12, right panel). Additionally, the pdfs of passive and vorticity increments for separations inside the inertial range collapse one onto the others (figure 13), signalling that the scaling exponents coincide: $\zeta_N^c = \zeta_N^a$. In summary,

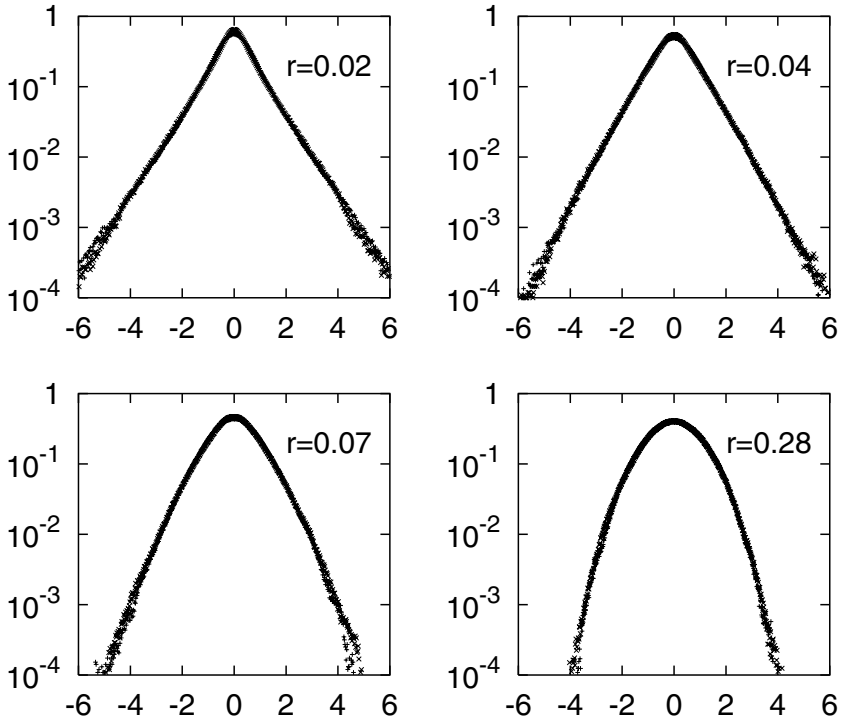

Figure 13. Pdfs of vorticity differences (+) and passive scalar ones (×), normalized by their respective standard deviation at different scales r within the scaling range.

the vorticity field and the passive scalar share the same statistical scaling properties [12, 16, 17], similar to the 2D convection case. However, differences may appear for odd-order moments [55].

It is now interesting to understand how the equivalence of active and passive statistics is realized: we shall see that, in this case, the smoothness of the flow is a crucial ingredient.

Let us start with the decaying passive scalar (42). First of all, it should be noted that the presence of non-zero friction ($\alpha > 0$) regularizes the field, and there is absence of dissipative anomaly [53], even if the mechanism is different from the MHD one. As a consequence, in equation (42), we can substitute $\kappa = 0$ and solve it by the method of characteristics (see section 2.2), i.e. $c(\boldsymbol{x}, t) = \int_{-\infty}^{t} \mathrm{d}s f_c(\boldsymbol{\rho}(s; \boldsymbol{x}, t), s) \exp(-\alpha(t-s))$, where now the path $\boldsymbol{\rho}(s; \boldsymbol{x}, t), s$ is unique due to the smoothness of the velocity field (note that $E_v(k) \sim k^{-3-\xi}$ is always steeper than k^{-3}; see also figure 12(left panel). The integral extends up to $-\infty$, where the initial conditions are set.

Passive scalar increments $\delta_r c = c(\boldsymbol{x}_1, t) - c(\boldsymbol{x}_2, t)$ (where $r = |\boldsymbol{x}_1 - \boldsymbol{x}_2|$), which are the objects we are interested in, are associated with particles pairs by the relation

$$\delta_r c = \int_{-\infty}^{t} \mathrm{d}s\, \mathrm{e}^{-\alpha(t-s)} [f_c(\boldsymbol{\rho}(s; \boldsymbol{x}_1, t), s) - f_c(\boldsymbol{\rho}(s; \boldsymbol{x}_2, t), s)]. \tag{43}$$

It should be mentioned here that the integrand $f_c(\boldsymbol{\rho}(s; \boldsymbol{x}_1, t), s) - f_c(\boldsymbol{\rho}(s; \boldsymbol{x}_2, t), s)$ stays small as long as the separation between the two paths remains below the forcing correlation scale ℓ_f, whereas for separations larger than ℓ_f, it is approximately equal to a Gaussian random variable X. In the latter statement, we used the independence between f_c and the particle trajectories,

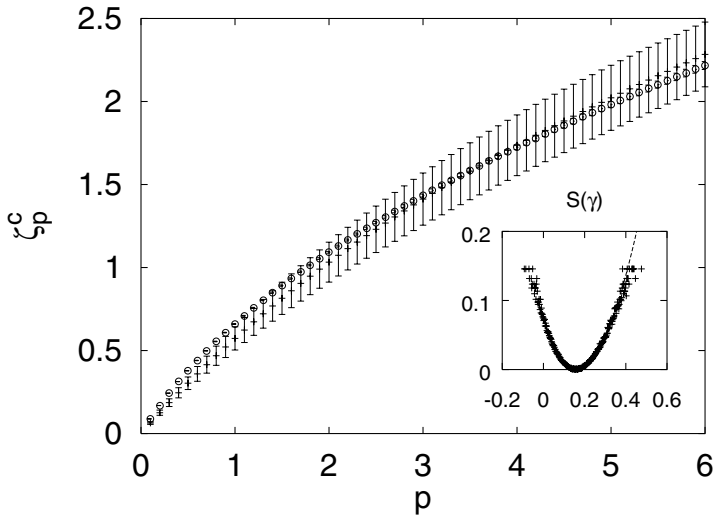

Figure 14. The scaling exponents of the passive scalar ζ_p^c (+), which have been computed also for noninteger moments, indeed equation (46), holds in general. We also show the exponents obtained from the separation times statistics ($\odot$) according to $\langle \exp[-\alpha p \mathcal{T}_{\ell_f}(r)] \rangle \sim r^{\zeta_p^c}$ with average over $\sim 2 \times 10^5$ couple of Lagrangian particles. The error bars were estimated by the rms fluctuation of the local slope. In the inset, we plot the Cramer function $S(\gamma)$, computed from finite-time Lyapunov exponents (symbols) and exit time statistics (line).

ensured by the passive nature of c. Therefore, equation (43) can be approximated as

$$\delta_r c \approx X \int_{-\infty}^{t-\mathcal{T}_{\ell_f}(r)} \mathrm{d}s\, \mathrm{e}^{-\alpha(t-s)} \sim X \mathrm{e}^{-\alpha \mathcal{T}_{\ell_f}(r)}, \tag{44}$$

where $\mathcal{T}_{\ell_f}(r)$ is the time necessary for the particles pair to go from r to ℓ_f backward in time. It is now clear that large fluctuations are associated with fast separating couples, $\mathcal{T}_{\ell_f}(r) \ll \langle \mathcal{T}_{\ell_f}(r) \rangle$, and small fluctuations with slow ones. Moreover, since $\boldsymbol{v}$ is smooth, 2D and incompressible, pairs separation is exponential and its statistics is described by a single finite-time Lyapunov exponent [56], γ. It is related to the separation time through the relation

$$\ell_f = r \mathrm{e}^{\gamma \mathcal{T}_{\ell_f}(r)}. \tag{45}$$

Large deviations theory states that, for large times, the random variable γ is distributed as $P(\gamma, t) \sim t^{1/2} \exp[-S(\gamma)t]$. $S(\gamma)$, the so-called Cramer function [57], is positive, concave and has a quadratic minimum, $S(\lambda) = 0$ in the maximum Lyapunov exponent λ. From (44) and (45), along with the expression for $P(\gamma, t)$, structure functions can be computed as

$$S_N^c(r) \sim \langle X^N \rangle \int \mathrm{d}\gamma \left(\frac{r}{\ell_f}\right)^{(N\alpha + S(\gamma))/\gamma} \approx \left(\frac{r}{\ell_f}\right)^{\zeta_N^c}, \tag{46}$$

where $\zeta_N^c = \min_\gamma \{N, [N\alpha + S(\gamma)]/\gamma\}$. Figure 14 shows that this prediction is verified by numerical simulations. The anomalous exponents, ζ_N^c, can therefore be evaluated in terms of the flow properties through the Cramer funtion $S(\gamma)$.

Since $\zeta_N^c = \zeta_N^a$, one may be tempted to apply straightforwardly the same argument to vorticity as that used for the passive scalar. However, the crucial assumption used in the derivation

of equation (46) is the statistical independence of particle trajectories and the forcing. That allows us to consider $\mathcal{T}_{\ell_f}(r)$ and X as independent random variables. Although this is obviously true for c, it is clear that the vorticity forcing f_a may influence the velocity statistics and, as a consequence, the particle paths. In other terms, for the vorticity field, we cannot *a priori* consider X and $\mathcal{T}_{\ell_f}(r)$ as independent.

Nevertheless, it is possible to support the validity of equation (43) for vorticity too. Indeed, the random variable $\mathcal{T}_{\ell_f}(r)$ is essentially determined by the evolution of the strain along the Lagrangian paths for times $t - \mathcal{T}_{\ell_f}(r) < s < t$, whereas X results from the scalar input accumulated at times $s < t - \mathcal{T}_{\ell_f}(r)$. Since the strain correlation time is basically α^{-1} for $\mathcal{T}_{\ell_f}(r) \gg \alpha^{-1}$, it is reasonable to assume that $\mathcal{T}_{\ell_f}(r)$ and X are statistically independent. Equation (45) allows us to translate the condition $\mathcal{T}_{\ell_f}(r) \gg \alpha^{-1}$ into $r \ll \ell_f \exp(-\gamma/\alpha)$ and to conclude that, at small scales, we can safely assume that the vorticity behaves as a passive field.

We conclude this section with two remarks. First, a difference between the present scenario and the one emerging from 2D convection should be pointed out. Here, the scaling exponents depend on the statistics of the finite-time Lyapunov exponents, which in turn depends on the way the vorticity is forced. As a consequence, universality may be lost. Secondly, the smoothness of the velocity field plays a central role in the argument used to justify the equivalence of the statistics of a and c in this system. For rough velocity fields, $\mathcal{T}_{\ell_f}(r)$ is basically independent of r for $r \ll \ell_f$ and the argument given in this section would not apply.

6. Turbulence on fluid surfaces

6.1. Surface quasi-geostrophic (SQG) turbulence

The study of geophysical fluids is of obvious importance for the understanding of weather dynamics and global circulation. Taking advantage of stratification and rotation, controlled approximations on the Navier–Stokes equations are usually performed to obtain more tractable models. For example, the motion of large portions of the atmosphere and ocean have a stable density stratification, i.e. lighter fluid sits above heavier one. This stable stratification, combined with the planetary rotation and the consequent Coriolis force, causes the most energetic motion to occur approximately in horizontal planes and leads to a balance of pressure gradients and inertial forces. This situation is mathematically described by the quasi-geostrophic equations [7, 8]. On the lower boundary, the surface of the earth or the bottom of the ocean, the vertical velocity has to be zero and this further simplifies the equations. Assuming that the fluid is infinitely high and the free surface is flat, the dynamics is then described by the SQG equation [9, 58]. It governs the temporal variations of the density field, our active scalar a throughout this section. For an ideal fluid, the density variation will be proportional to the temperature variation and one can use the potential temperature as the fundamental field.

The density fluctuations evolve according to the transport equation

$$\partial_t a + \boldsymbol{v} \cdot \nabla a = \kappa \Delta a + f_a, \tag{47}$$

and the velocity field is functionally related to a. In terms of the stream function ψ, the density a is obtained as $a(\boldsymbol{x}, t) = (-\Delta)^{1/2}\psi(\boldsymbol{x}, t)$ and $\boldsymbol{v} = (\partial_y, -\partial_x)\psi$. In Fourier space, the link is particularly simple

$$\hat{\boldsymbol{v}}(\boldsymbol{k}, t) = -\mathrm{i}\left(\frac{k_y}{k}, -\frac{k_x}{k}\right)\hat{a}(\boldsymbol{k}, t). \tag{48}$$

In the early days of computer simulations, equations (47) and (48) had been used for weather forecasting. Recently, they have attracted renewed interest in view of their formal analogy with the 3D Navier–Stokes equations [59, 60], and as a model of active scalar [9, 10].

It is instructive to generalize (48) as

$$\hat{\boldsymbol{v}}(\boldsymbol{k}, t) = -\mathrm{i}\left(\frac{k_y}{k^z}, -\frac{k_x}{k^z}\right)\hat{a}(\boldsymbol{k}, t). \tag{49}$$

For $z = 1$, one recovers (48), whereas $z = 2$ corresponds to the 2D Navier–Stokes equation and a is the vorticity (see the previous section). The value of z tunes the degree of *locality*. The case of interest here is $z = 1$, corresponding to the same degree of locality as in $3d$ turbulence [9].

Equations (47) and (49) have two inviscid unforced quadratic invariants, $E = -\int \mathrm{d}\boldsymbol{x}\, a\psi$ and $\Omega = \int \mathrm{d}\boldsymbol{x}\, a^2$, which, for $z = 2$, correspond to the energy and the enstrophy, respectively. Notice that, for $z = 1$, the fields $\boldsymbol{v}$ and a have the same dimension and $E_a(k) \equiv E_v(k)$. Quasi-equilibrium arguments predict an inverse cascade of E and a direct cascade of Ω. If k_f identifies the injection wave number, dimensional arguments give the expected spectral behaviour [9]:

$$E_a(k) \propto \begin{cases} k^{-7/3+(4z/3)}, & k \ll k_f, \\ k^{-7/3+(2z/3)}, & k \gg k_f. \end{cases} \tag{50}$$

For $z = 2$, one recovers the 2D Navier–Stokes expectation [50, 51]. Here, we are interested in the range $k > k_f$ and $z = 1$, so that $E_a(k) \equiv E_v(k) \sim k^{-5/3}$ as in $3d$ turbulence. Assuming the absence of intermittency, the spectrum $E_v(k) \sim k^{-5/3}$ would imply $\delta_r v \sim r^{1/3}$. Therefore, for a passive scalar, one expects the standard phenomenology: an intermittent direct cascade with $E_c(k) \sim k^{-5/3}$ to the Oboukov–Corrsin–Kolmogorov type of arguments [4].

6.1.1. Direct numerical simulations settings. We performed a set of high-resolution direct numerical simulations of equations (47) and (48) along with the passive scalar equation (2). Integration has been performed by means of a $\frac{2}{3}$-de-aliased pseudo-spectral method on a $2\pi \times 2\pi$ doubly periodic square domain with $\mathcal{N}^2$ collocation points. Time integration has been performed with a second-order Adam–Bashforth or Runge–Kutta algorithm, appropriately modified to integrate exactly the dissipative terms. The latter ones, as customary, have been replaced by a hyperdiffusive term, which, in Fourier space, reads $-k^{2p}\hat{a}(\boldsymbol{k}, t)$. Since the system is not stationary owing to the inverse cascade of E, we added an energy sink at large scales of the form $-k^{-q}\hat{a}(\boldsymbol{k}, t)$. To evaluate its possible effect on inertial quantities, a very-high-resolution (4096^2) DNS has been performed without any energy sink at large scales.

A summary of the numerical settings can be found in table 1. We considered different scalar inputs: (G) a δ-correlated forcing as defined in equation (23) with Gaussian correlation function; (B) same as above, but with forcing restricted to a few wavenumbers shells as in equation (27); (NG) a non-Gaussian finite-time correlated forcing to produce non-zero three-point correlations for the scalar fields (see section 6.3 for a detailed discussion).

6.2. Active and passive scalar statistics in SQG turbulence

Let us first study the measured scalar spectra to check the dimensional predictions. In figure 15, we summarize the spectral behaviour for a and c in two different simulations (i.e. runs 1 and 3).

Table 1. Summary of the settings in DNS.

Run	$\mathcal{N}^2$	p	q	F	k_f
1	4096^2	2		B	44–48
2	2048^2	2	1/2	B	2–6
3	2048^2	2	0	G	5
4	2048^2	2	1/2	G	5
5	2048^2	2	0	NG	5

Note: Runs 1 and 2 are forced according to equation (23), and run 1 is without any friction term. Runs 3 and 4 are forced according to equation (27). Run 5 is forced with the non-Gaussian forcing discussed in section 6.3. Lower (512^2) resolution runs under several settings both for the dissipative and friction terms were also performed.

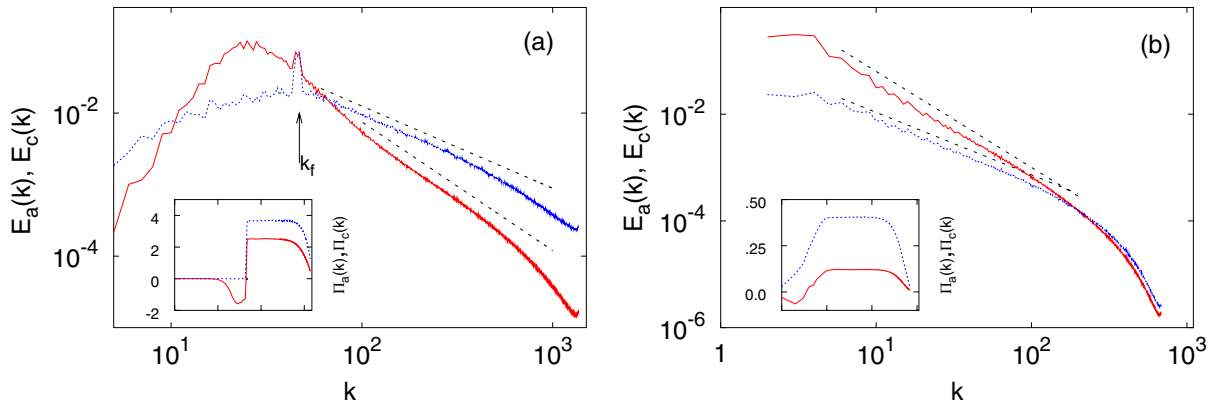

Figure 15. (a) Power spectra of the active (red) and passive (blue) scalar variances, $E_a(k) = \pi k|\hat{a}(\boldsymbol{k}, t)|^2$ and $E_c(k) = \pi k|\hat{c}(\boldsymbol{k}, t)|^2$, for run 1; the inset shows the active and passive energy fluxes $\Pi_{a,c}(k)$. The dashed lines indicates the best-fitted spectral slopes $E_a(k) \sim k^{-1.8\pm0.1}$ and $E_c(k) \sim k^{-1.15\pm0.05}$. Note that the fitted slope for $E_a(k)$ is better recovered at higher wavenumbers; close to the energy peak a steeper spectrum ($\sim k^{-2\pm0.1}$) is observed. (b) Same as (a) but for run 3. The inset shows the scalar fluxes. The dashed lines indicates the spectral slopes $E_a(k) \sim k^{-1.8\pm0.1}$ and $E_c(k) \sim k^{-1.17\pm0.05}$. Here, the scaling range is wider than that in run 1. For both runs, active and passive spectra have been shifted for visualization purposes. In the other runs, we observe the same qualitative and quantitative features within the error bars. In particular, runs 1 and 2 give almost indistinguishable spectral slopes, meaning that the large-scale energy sink does not enter too much into the inertial range, which is as expected since the velocity field is rough at small scales. Run 5 produced spectral slopes indistinguishable from those of runs 3 and 4. However, it should be noted that runs 1 and 2 display a steeper spectra close to the forcing wavenumbers; this feature is absent from the other runs and may be due to finite-size effects (see text and also figure 17).

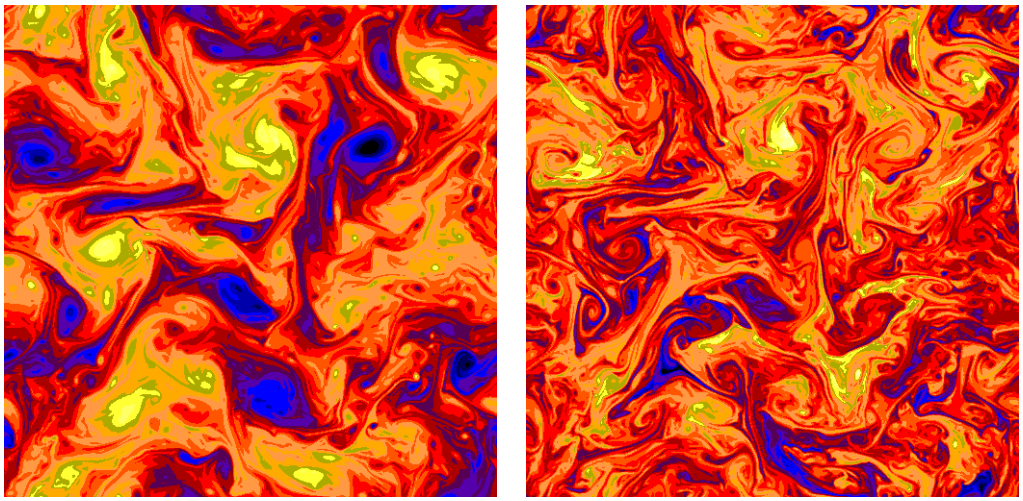

Figure 16. Snapshots of the active (left) and passive (right) scalars (at 512^2 resolution). Note the presence of coherent structures in the active field, which are slow-evolving. The passive field displays filament-like features, indicating that it is more rough compared with the active one.

Two observations are in order:

- The scalar spectra $E_a(k)$ is steeper than the dimensionally expected $k^{-5/3}$. The slope does not seem to depend on the injection mechanism.
- The active and passive scalars, both performing a direct cascade, are different already at the level of the spectral slopes. In particular, c is much rougher than a.

The differences between a and c are evident also from figure 16, where two simultaneous snapshots of the fields are displayed. A direct inspection of the fields confirms that c is more rough compared with a, and resembles a passive scalar in a smooth flow. Moreover, in a, we observe the presence of large coherent structures at the scale of the forcing. These are actually long-lived, slow-evolving structures that strongly impair the convergence of the statistics for high-order structure functions. Hence, in the following, we limit ourselves to a comparison of the low-order statistics of a and c, but this is sufficient to appreciate the differences beween active and passive scalar statistics.

The deviation from the dimensional expectation for the spectral slope of the active field was already observed in previous numerical studies [9], and it is possibly due to intermittency in the active scalar and velocity statistics. Indeed, the rescaled pdfs of the increments do not collapse (not shown). Concerning the universality of anomalous exponents with respect to the forcing statistics, we observe that the spectral slopes do not depend sensitively on the forcing statistics. However, the forcing (B) (see table 1) induces a steeper spectrum close to the forcing scale, whereas a universal slope is apparently recovered at large wavenumbers (figure 15(a)). The scaling of $S_2^a(r)$ seems to be more sensitive to the forcing (see figure 17). These discrepancies may be due to finite-size effects; these are more severe for the forcing (B), which is indeed characterized by a slower decay of the spatial correlations. Unfortunately, it is difficult to extract reliable information on the high-order statistics. Indeed, the presence of slowly evolving coherent

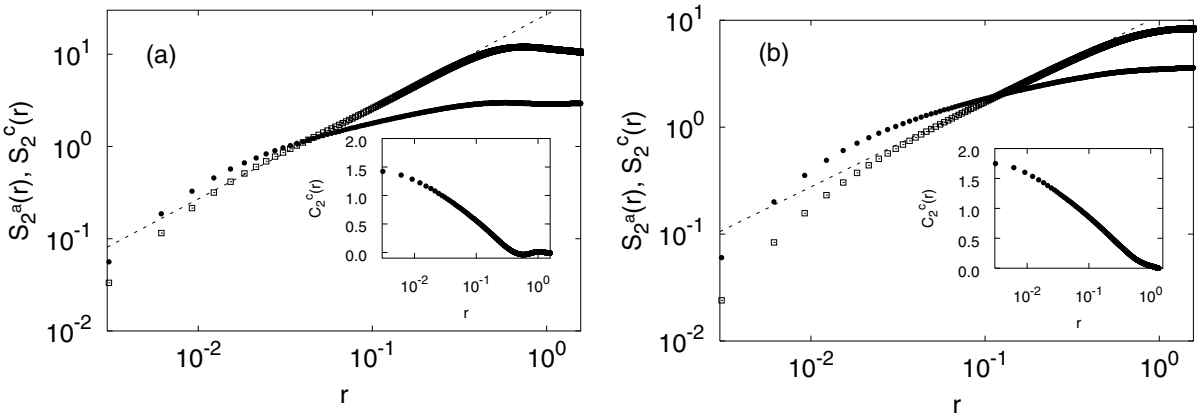

Figure 17. (a) Second-order structure function for the active (□) and the passive (●) scalars in run 2. The straight line shows the scaling $\sim r^1$ for the $S_2^a(r)$ (the same exponent is observed in run 1). The passive scalar does not display a neat scaling behaviour. In the inset, we show the correlation function for the passive scalar $\mathcal{C}_2^c(r)$ in log-lin scale (see text). (b) Same as (a) but for run 3. Here, the straight dashed line indicates the slope $r^{0.8}$. $S_2^a(r)$ in run 5 has a slope $\sim r^{0.84}$, compatible with the ones observed in runs 3 and 4 within statistical errors.

structures induces a poorly converging statistics for high-order structure functions. Therefore, we cannot rule out the possibility of dependence of the active scalar exponents on forcing statistics.

A result that emerges beyond any doubt is that active and passive scalars behave differently, as shown in figures 15–17. This is confirmed by the differences in the pdfs of $\delta_r a$ and $\delta_r c$ at various scales within the inertial range (figure 18). The single-point pdfs of a and c are different as well (not shown).

It is worth noting that the behaviour of the passive scalar deviates from naive expectations. We observe $E_c(k) \sim k^{-1.15}$, whereas a dimensional argument based on the observed velocity spectrum ($E_v(k) \equiv E_a(k) \sim k^{-1.8}$) and on the Yaglom relation [4] ($\langle \delta_r v\, (\delta_r c)^2 \rangle \sim r$) would yield $E_a(k) \sim k^{-1.6}$. The violation of the dimensional prediction is even more striking looking at $S_2^c(r)$ in figure 17. This feature is reminiscent of some experimental investigations of passive scalars in turbulent flows (see e.g. [61, 62] and references therein), where shallow scalar spectra are observed for the scalar even at those scales where the velocity field displays a K41 spectrum. It is probable that the presence of coherent structures (see figure 16) leads to persistent regions where the velocity field has a smooth (shear-like) behaviour. This suggests a two-fluid picture: a slowly evolving shear-like flow, with superimposed faster turbulent fluctuations. Under those conditions, one may expect that the particle pairs separate faster than expected, leading to shallower passive scalar spectra [63].

In conclusion, even though both passive and active scalars perform a direct cascade, their statistical properties are definitely different.

6.3. Scaling and geometry

Let us now compare the two scalar fields by investigating the three-point correlation functions of the active field $\mathcal{C}_3^a(\boldsymbol{x}_1, \boldsymbol{x}_2, \boldsymbol{x}_3) = \langle a(\boldsymbol{x}_1, t) a(\boldsymbol{x}_2, t) a(\boldsymbol{x}_3, t) \rangle$ and of the passive field $\mathcal{C}_3^c(\boldsymbol{x}_1, \boldsymbol{x}_2, \boldsymbol{x}_3) = \langle c(\boldsymbol{x}_1, t) c(\boldsymbol{x}_3, t) c(\boldsymbol{x}_3, t) \rangle$. This will allow us to assess the scaling properties of the correlation

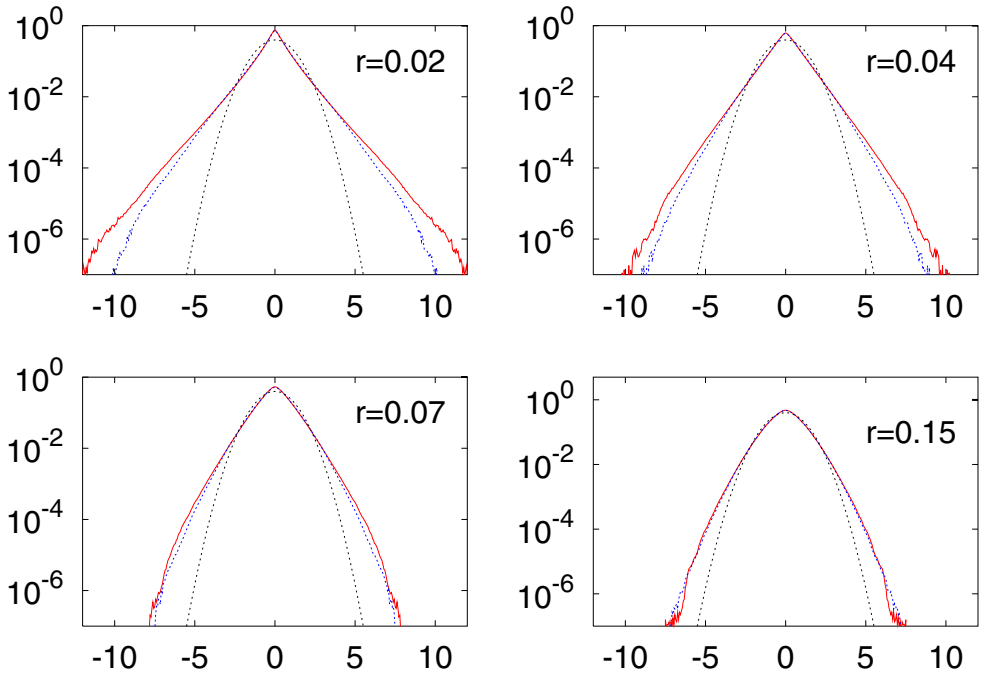

Figure 18. Pdfs of active (red) and passive (blue) scalar differences normalized by their respective standard deviations for four different scales within the inertial range. The dotted lines are Gaussian pdfs drawn for comparison. Data refer to run 3 and the other runs showed similar results.

function by measuring the dependence, on the global size, of the triangle identified by the three points, $R^2 = \sum_{i<j} x_{ij}^2$ (where $x_{ij} = |\boldsymbol{x}_i - \boldsymbol{x}_j|$). We will also investigate the geometrical dependence of C_3.

It has to be noted that for δ-correlated Gaussian forcings such as (23) and (27), $\mathcal{C}_3^a$ and $\mathcal{C}_3^c$ are both zero. Therefore, we need a different forcing statistics to study three-point correlations. One possibility is to break the rotational symmetry of the system by an anisotropic forcing, e.g. a mean gradient (24) as in [26]. However, that choice leads inevitably to $a = c$: the equations are identical for a and c so that the difference field $a - c$ will decay out. We then choose to force the system as follows. The two inputs f_a and f_c are

$$f_{a,c}(\boldsymbol{x}, t) = g_{a,c}^2(\boldsymbol{x}, t) - \int \mathrm{d}\boldsymbol{y}\, g_{a,c}^2(\boldsymbol{y}, t), \tag{51}$$

where $g_{a,c}$ is a homogeneous, isotropic and Gaussian random field with correlation

$$\langle g_i(\boldsymbol{x}, t) g_j(\boldsymbol{x}', t')\rangle = \delta_{i,j}\mathcal{G}(|\boldsymbol{x} - \boldsymbol{x}'|/\ell_f)\mathrm{e}^{-|t-t'|/\tau_f}, \tag{52}$$

where $i, j = a, c$; ℓ_f is the forcing scale, τ_f the forcing correlation time and $\mathcal{G}(r) \propto G_0 \exp(-r^2/2)$. The time correlation is imposed by performing an independent Ornstein–Uhlenbeck process at each Fourier mode, i.e. integrating the stochastic differential equation $\mathrm{d}\hat{g}_i(\boldsymbol{k}, t) = -1/\tau_f \hat{g}_i(\boldsymbol{k}, t)\,\mathrm{d}t + \sqrt{2G_0\,\mathrm{d}t/\tau_f}\,\mathrm{d}w_i(\boldsymbol{k}, t)$, where $\mathrm{d}w_i$ are zero mean Gaussian variables with $\langle \mathrm{d}w_i(\boldsymbol{k}, t)\,\mathrm{d}w_j(\boldsymbol{k}', t')\rangle = \delta_{i,j}\delta(t - t')\delta(\boldsymbol{k} - \boldsymbol{k}')$. If $\tau_f \ll \mathcal{T}_{\ell_f}$ by the central limit theorem, a Gaussian statistics is recovered. Therefore, we fixed $\tau_f \sim O(\mathcal{T}_{\ell_f})$ in our DNS. The

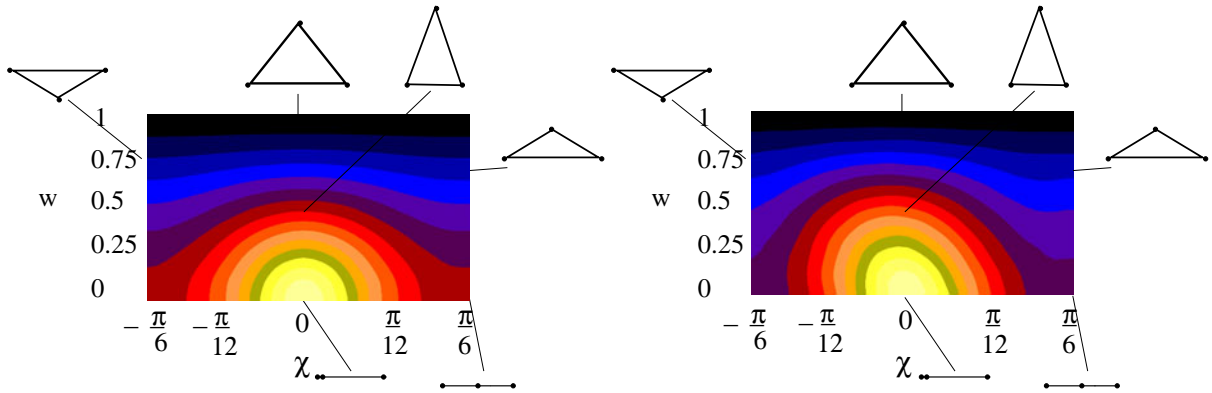

Figure 19. Contour plots in the χ–w plane of the three-point shape function, Φ, for passive (left) and active (right) scalar.

advantages of this choice are that it preserves the isotropy and gives analytical control on the forcing correlation functions.

Let us now see how the triangle identified by the three points, $\underline{\boldsymbol{x}} = (\boldsymbol{x}_1, \boldsymbol{x}_2, \boldsymbol{x}_3)$, can be parameterized. In two dimensions, we need $3d = 6$ variables to define a triangle. Since the correlation functions should possess all the statistical symmetries of the system, the number of degrees of freedom is reduced. In particular, translational invariance ensures no dependence on the position of the centre of mass of the triangle, $(\boldsymbol{x}_1 + \boldsymbol{x}_2 + \boldsymbol{x}_3)/3$. The correlation function is thus a function of the separation vectors among the three points, i.e. $\mathcal{C}_3^{a,c}(\underline{\boldsymbol{x}}) = \mathcal{C}_3^{a,c}(\boldsymbol{x}_{12}, \boldsymbol{x}_{23}, \boldsymbol{x}_{31})$. Additionally, isotropy implies that a rigid rotation of the triangle has no effect on the value of C_3, so that three variables suffice: the global size of the triangle R and two parameters that define its shape. In terms of the Euler parametrization [64]–[66], upon defining $\boldsymbol{\rho}_1 = (\boldsymbol{x}_1 - \boldsymbol{x}_2)/\sqrt{2}$ and $\boldsymbol{\rho}_2 = (\boldsymbol{x}_1 + \boldsymbol{x}_2 - 2\boldsymbol{x}_3)/\sqrt{6}$, the shape of the triangle is given in terms of these two variables:

$$w = \frac{2\boldsymbol{\rho}_1 \times \boldsymbol{\rho}_2}{R^2} \qquad \chi = \frac{1}{2}\tan^{-1}\left[\frac{2\boldsymbol{\rho}_1 \cdot \boldsymbol{\rho}_2}{\rho_1^2 - \rho_2^2}\right], \tag{53}$$

where $|w|$ is the ratio of the area of the triangle to the area of the equilateral triangle having the same size, $R^2 = \rho_1^2 + \rho_2^2$. χ has no simple geometrical interpretation. Some shapes corresponding to a few (w, χ) are shown in figure 19.

The three-point correlation function can be decomposed as [25, 29]

$$\mathcal{C}_3^{a,c}(\underline{\boldsymbol{x}}) = \mathcal{R}\{\mathcal{C}_3^{a,c}(\underline{\boldsymbol{x}})\} + \mathcal{I}\{\mathcal{C}_3^{a,c}(\underline{\boldsymbol{x}})\}, \tag{54}$$

where $\mathcal{R}, \mathcal{I}$ are the reducible and irreducible components, respectively. This means that $\mathcal{C}_3$ can be expressed as the sum of one part that depends on three points (hereafter denoted as C_3) and another part that depends on two points (hereafter denoted C_2), i.e. $\mathcal{C}_3(\boldsymbol{x}_1, \boldsymbol{x}_2, \boldsymbol{x}_3) = C_3(\boldsymbol{x}_1, \boldsymbol{x}_2, \boldsymbol{x}_3) + C_2(\boldsymbol{x}_1, \boldsymbol{x}_2) + C_2(\boldsymbol{x}_2, \boldsymbol{x}_3) + C_2(\boldsymbol{x}_3, \boldsymbol{x}_1)$. The reducible part, $\mathcal{R}\{\mathcal{C}_3\} = C_2(\boldsymbol{x}_1, \boldsymbol{x}_2) + C_2(\boldsymbol{x}_2, \boldsymbol{x}_3) + C_2(\boldsymbol{x}_3, \boldsymbol{x}_1)$, and the irreducible part, $\mathcal{I}\{\mathcal{C}_3\} = C_3(\boldsymbol{x}_1, \boldsymbol{x}_2, \boldsymbol{x}_3)$, are generally characterized by different scaling properties as a function of the triangle size R and different geometrical (shape) dependencies [26, 67].

In terms of the variables R, w and χ, the reducible and irreducible components take the following form:

$$\begin{aligned} \mathcal{R}\{\mathcal{C}_3^{a,c}(\underline{\boldsymbol{x}})\} &= h_{a,c}^{\mathcal{R}}(R)\Phi_{a,c}^{\mathcal{R}}(\chi, w), \\ \mathcal{I}\{\mathcal{C}_3^{a,c}(\underline{\boldsymbol{x}})\} &= h_{a,c}^{\mathcal{I}}(R)\Phi_{a,c}^{\mathcal{I}}(\chi, w), \end{aligned} \tag{55}$$

where the function $h(R)$ is expected to have a scaling dependence over the inertial range.

For the passive scalar, the scaling behaviour of the reducible part $h_c^{\mathcal{R}}(R)$ is dominated by the dimensional scaling imposed by the balance with the forcing, whereas the scaling of the irreducible part $h_c^{\mathcal{R}}(R)$ is given by the zero modes [29]. With a finite-correlated pumping, the forcing statistics may, in principle, contribute to the irreducible part [25]; however, in our study, these hypothetical contributions appear to be small, if not absent. For the active scalar, it is not possible to make any *a priori* argument to predict the scaling behaviour of the reducible and irreducible parts. As far as the geometrical dependence is concerned, i.e. $\Phi_c^{\mathcal{R},I}$ and $\Phi_a^{\mathcal{R},I}$, it is very difficult to separate the two contributions. In our case, in agreement with the results obtained for the Kraichanan model [67], the reducible part turns out to be the leading contribution, so that we only present the shape dependence of the full correlation functions, which basically coincides with the reducible one. Hereafter, we will use $\Phi_{a,c}$, dropping the indices that distinguish the two contributions.

Let us start by studying the shape dependence of the correlation function for the active, $\Phi_a(\chi, w)$, and passive scalars, $\Phi_c(\chi, w)$. Exploiting the invariance under arbitrary permutations of the three vertices of the triangle, we can reduce the configuration space to $\chi \in [-\pi/6 : \pi/6]$, and to $w \in [0 : 1]$, going from degenerate (collinear points) to equilateral triangles. The function $\Phi(\chi, w)$ is anti-periodic in χ with period $\pi/3$ [64]–[66]. The functions Φ_c and Φ_c are shown in figure 19. They have been measured for a fixed size R within the inertial range. The two functions display similar qualitative features: the intensity increases going from equilateral to collinear triangles, and the maximum is realized for almost degenerate triangles $(\chi, w) = (0, 0)$. Φ_c is invariant for $\chi \to -\chi$, which corresponds to reflection with respect to an axis. This symmetry is owing to the equation of motion and the fact that $f_c \to f_c$ under this symmetry transformation. The active scalar displays a weak breaking of this symmetry, because it is a pseudoscalar, whereas f_a is not.

Let us now turn our attention to the scaling behaviour. Since the reducible scaling behaviour is the leading one, it is simply obtained by fixing a certain shape for the triangle (we did for several choices of (χ, w)) and varying its size. The results are shown in figure 20(a). We observed that $h_a^{\mathcal{R}}(R)$ and $h_c^{\mathcal{R}}(R)$ are different. Moreover, whereas $h_c^{\mathcal{R}}(R)$ is practically parallel with $S_2^c(R)$, we observe for the active scalar that $h_a^{\mathcal{R}}(R)$ is not scaling as $S_2^a(R)$.

The measure of the subleading, irreducible part is more involved, and we proceed as follows. We fix a reference triangle shape (χ, w) and set the origin at the centre of mass of the triangle. Now $\boldsymbol{x}_i$ indicates the position of vertex i of the triangle. We define $\hat{d}_1 = \hat{d}_1(\lambda)$ (where $\lambda \geqslant 1$) as the dilation operator that transforms the triangle $(\boldsymbol{x}_1, \boldsymbol{x}_2, \boldsymbol{x}_3)$ in $(\lambda\boldsymbol{x}_1, \boldsymbol{x}_2, \boldsymbol{x}_3)$. Analogous definitions hold for the other vertices. Obviously, $\hat{d}_i(1) \equiv \hat{I}$ is the identity. We then consider the composite operator $\hat{\mathcal{D}}(\lambda) = \hat{d}_1\hat{d}_2\hat{d}_3 - \hat{d}_1\hat{d}_2 - \hat{d}_2\hat{d}_3 - \hat{d}_3\hat{d}_1 + \hat{d}_1 + \hat{d}_2 + \hat{d}_3 - \hat{I}$. By direct substitution, it is easily seen that, in $\hat{\mathcal{D}}(\lambda)\mathcal{C}_3(\boldsymbol{x}_1, \boldsymbol{x}_2, \boldsymbol{x}_3)$, all the reducible terms are cancelled, and only a linear superposition of terms involving the irreducible parts survives. Therefore, the average of $\hat{\mathcal{D}}(\lambda)c(\boldsymbol{x}_1)c(\boldsymbol{x}_2)c(\boldsymbol{x}_3)$ for triangles of different sizes R, but of fixed shape (χ, w), will give the scaling of the irreducible part of the three-point function (55). A similar procedure has been used for a. We used as the reference configuration a collinear triangle with two degenerate vertices, i.e. $(\chi, w) = (0, 0)$. This choice decreases the number of cancellations. Additionally, this configuration corresponds to the region of stronger gradients in the function Φ (see figure 19), yielding a higher signal-to-noise ratio. By varying λ, we tested the robustness of the measured scaling.

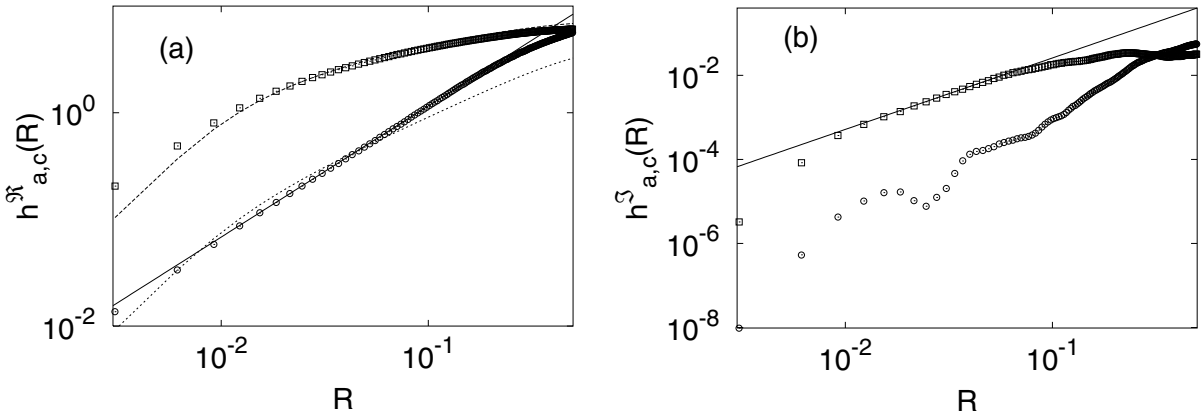

Figure 20. (a) $h^{\mathcal{R}}(R)$ versus R for the active (○) and passive (□) scalar. The dashed lines are the second-order structure functions, $S_2^{a,c}$, multiplied by a factor to allow for a comparison. The solid line gives the fitted slope, $R^{1.23\pm0.05}$, for $h_a^{\mathcal{R}}(R)$. The slope of S_2^a is $\approx r^{.84\pm0.05}$ and is compatible with those obtained with the forcing (G), see figure 17. The passive curves have been shifted for visualization purposes. (b) $h_{a,c}^{\mathcal{I}}(R)$ versus R for the active (○) and passive (□) scalar. For c the scaling $R^{1.7\pm0.2}$ (solid line) is measured. The signal for the active scalar is very low and no scaling behaviour can be detected. The statistics has been computed averaging over about 65 frames separated by half eddy turnover time.

In figure 20, we present our results on the scale dependence of $h_c^{\mathcal{I}}(R)$ and $h_a^{\mathcal{I}}(R)$. Clearly, $h_a^{\mathcal{I}}(R)$ has too low a signal to identify any scaling behaviour, whereas the passive scalar scales fairly well, and we measured $h_c^{\mathcal{I}}(R) \sim R^{1.7}$, confirming that the irreducible part is subleading.

A couple of final remarks are in order. First, the fact that $h_a^{\mathcal{R}}(R)$ does not scale as $S_2^a(R)$ is the signature of the correlations between f_a and the particle propagator. Indeed, for the passive scalar, $h_c^{\mathcal{R}}(R) \propto S_2^c(R)$ is a straightforward consequence of the independence of $\boldsymbol{v}$ and f_c. Secondly, $h_a^{\mathcal{R}}(R)$ scales differently from $h_c^{\mathcal{I}}(R)$: this rules out the possibility of establishing simple relationships between active and passive scalar statistics (see [15] for a related discussion).

7. Conclusions and perspectives

In summary, we have investigated the statistics of active and passive scalars transported by the same turbulent flow. We put the focus on the issue of universality and scaling. In this respect, the passive scalar problem is essentially understood. Conversely, the active case is, by far and away, a challenging open problem. The basic property that make passive scalar turbulence substantially simpler is the absence of statistical correlations between scalar forcing and carrier flow. In contrast, the hallmark of active scalars is the functional dependence of velocity on the scalar field and, thus, on active scalar pumping. Yet, when correlations are sufficiently weak, the active scalar behaves in a similar manner as the passive one: this is the case of 2D thermal convection and Ekman turbulence. However, this appears to be a nongeneric situation, and the equivalence between passive and active scalars is rooted in special properties of those systems. Indeed, different systems such as 2D MHD and SQG turbulence are characterized by a marked difference between passive and active scalar statistics. This poses the problem of universality

in active scalar turbulence: if the forcing is capable of influencing the velocity dynamics, how can scaling exponents be universal with respect to the details of the injection mechanism? So far, a satisfactory answer is missing. As of today, numerical experiments favour the hypothesis that universality is not lost in a number of active scalars, but further investigation is needed to elucidate this fundamental issue.

Acknowledgments

We are grateful to G Boffetta, S Musacchio and T Matsumoto for their partial collaboration in the material presented here. We thank T Gilbert, A Noullez and I Procaccia for useful discussions. This work has been partially supported by the European Union under the contracts HPRN-CT-2000-00162 and HPRN-CT-2002-00300, and by Indo–French Center for Promotion of Advanced Research (IFCPAR 2404-2). AM and MC have been partially supported by Cofin2003 ('Sistemi Complessi e Problemi a Molti Corpi'). MC has been partially supported by the European Union under the contract HPRN-CT-2000-00162, and acknowledges the Max Planck Institute for the Physics of Complex Systems (Dresden) for computational resources. Numerical simulations have been performed at IDRIS (project 021226) and at CINECA (INFM parallel computing initiative).

References

[1] Pasquill F and Smith F B 1983 *Atmospheric Diffusion* (Chichester: Ellis Horwood)
[2] Williams F A 1985 *Combustion Theory* (Menlo Park, CA: Benjamin-Cummings)
[3] Zel'dovich Ya B, Ruzmaikin A and Sokoloff D 1983 *Magnetic Fields in Astrophysics* (New York: Gordon and Breach)
[4] Monin A and Yaglom A 1975 *Statistical Fluid Mechanics* (Cambridge, MA: MIT Press)
[5] Siggia E D 1994 *Ann. Rev. Fluid Mech.* **26** 137
[6] Biskamp D 1993 *Nonlinear Magnetohydrodynamics* (Cambridge: Cambridge University Press)
[7] Salmon R 1998 *Geophysical Fluid Dynamics* (New York: Oxford University Press)
[8] Rhines P B 1979 *Ann. Rev. Fluid Mech.* **11** 401
[9] Pierrehumbert R T, Held I M and Swanson K L 1994 *Chaos Sol. Fract.* **4** 1111
Held I M, Pierrehumbert R T, Garner S T and Swanson K L 1995 *J. Fluid Mech.* **282** 1
[10] Constantin P 1998 *J. Stat. Phys.* **90** 571
[11] Celani A, Matsumoto T, Mazzino A and Vergassola M 2002 *Phys. Rev. Lett.* **88** 054503
[12] Boffetta G, Celani A, Musacchio A and Vergassola M 2002 *Phys. Rev.* E **66** 026304
[13] Celani A, Cencini M, Mazzino A and Vergassola M 2002 *Phys. Rev. Lett.* **89** 234502
[14] Ching E S C, Cohen Y, Gilbert T and Procaccia I 2002 *Europhys. Lett.* **60** 369
[15] Ching E S C, Cohen Y, Gilbert T and Procaccia I 2003 *Phys. Rev.* E **67** 016304
[16] Nam K, Antonsen T M, Guzdar P N and Ott E 1999 *Phys. Rev. Lett.* **83** 3426
[17] Nam K, Ott E, Antonsen T M and Guzdar P N 2000 *Phys. Rev. Lett.* **84** 5134
[18] Frisch U 1995 *Turbulence: The Legacy of A. N. Kolmogorov* (Cambridge: Cambridge University Press)
[19] Celani A, Lanotte A, Mazzino A and Vergassola M 2000 *Phys. Rev. Lett.* **84** 2385
Celani A, Lanotte A, Mazzino A and Vergassola M 2001 *Phys. Fluids* **13** 1768
[20] Kraichnan R H 1968 *Phys. Fluids* **11** 945
[21] Kraichnan R H 1994 *Phys. Rev. Lett.* **72** 1016
[22] Gawędzki K and Kupiainen A 1995 *Phys. Rev. Lett.* **75** 3834
[23] Chertkov M, Falkovich G, Kolokolov I and Lebedev V 1995 *Phys. Rev.* E **52** 4924

[24] Shraiman B I and Siggia E D 1995 *C. R. Acad. Sci. Paris Série II* **321** 279
[25] Falkovich G, Gawędzki K and Vergassola M 2001 *Rev. Mod. Phys.* **73** 913
[26] Celani A and Vergassola M 2001 *Phys. Rev. Lett.* **86** 424
[27] Frisch U, Mazzino A, Noullez A and Vergassola M 1999 *Phys. Fluids* **11** 2178
[28] Risken H 1998 *The Fokker Planck Equation* (Berlin: Springer)
[29] Bernard D, Gawędzki K and Kupiainen A 1998 *J. Stat. Phys.* **90** 519
[30] Arad I, Biferale L, Celani A, Procaccia I and Vergassola M 2001 *Phys. Rev. Lett.* **87** 164502
[31] Chertkov M, Kolokolov I and Vergassola M 1997 *Phys. Rev.* E **56** 5483
[32] Gawędzki K and Vergassola M 2000 *Physica* D **138** 63
[33] Yakhot V 1997 *Phys. Rev.* E **55** 329
[34] Bizon C, Werne J, Predtechensky A A, Julien K, McCormick W D, Swift J B and Swinney H L 1997 *Chaos* **7** 1
[35] Rivera M and Wu X L 2000 *Phys. Rev. Lett.* **85** 976
[36] Celani A, Mazzino A and Vergassola M 2001 *Phys. Fluids* **13** 2133
[37] Warhaft Z 2000 *Annu. Rev. Fluid Mech.* **32** 203
[38] Moisy F, Willaime H, Andersen J S and Tabeling P 2001 *Phys. Rev. Lett.* **86** 4827
[39] Zhou S-Q and Xia K-Q 2002 *Phys. Rev. Lett.* **89** 184502
[40] Antonelli M, Mazzino A and Rizza U 2003 *J. Atmos. Sci.* **60** 215
[41] Paret J and Tabeling P 1998 *Phys. Fluids* **10** 3126
[42] Boffetta G, Celani A and Vergassola M 2000 *Phys. Rev.* E **61** R29
[43] Pouquet A 1978 *J. Fluid. Mech.* **88** 1
[44] Biskamp D and Bremer U 1994 *Phys. Rev. Lett.* **72** 3819
[45] Celani A, Cencini M and Noullez A 2004 *Preprint* physics/0305058; *Physica* D, to appear
[46] Sridhar S and Goldreich P 1994 *Astrophys. J.* **432** 612
[47] Verma M K, Roberts D A, Goldstein M L, Ghosh S and Stribling W T 1996 *J. Geophys. Res.* **101** 21619
[48] Politano H, Pouquet A and Carbone V 1998 *Europhys. Lett.* **43** 516
[49] Biskamp D and Schwarz E 2001 *Phys. Plasmas* **8** 3282
[50] Kraichnan R H 1967 *Phys. Fluids* **10** 1417
[51] Batchelor G K 1969 *Phys. Fluids* **12** (Suppl. II) 233
[52] Paret J, Jullien M C and Tabeling P 1999 *Phys. Rev. Lett.* **83** 3418
[53] Chertkov M 1999 *Phys. Fluids* **11** 2257
[54] Jullien M C, Castiglione P and Tabeling P 2000 *Phys. Rev. Lett.* **85** 3636
[55] Bernard D 2000 *Europhys. Lett.* **50** 333
[56] Crisanti A, Paladin G and Vulpiani A 1993 *Products of Random Matrices* (Berlin: Springer)
[57] Ellis R S 1985 *Entropy, Large Deviations, and Statistical Mechanics* (New York: Springer)
[58] Constantin P 2002 *Phys. Rev. Lett.* **89** 184501
[59] Constantin P 1995 *Physica* D **86** 212
[60] Majda A and Tabak E 1996 *Physica* D **98** 515
[61] Villermaux E, Innocenti C and Duplat J 2001 *Phys. Fluids* **13** 284
[62] Villermaux E and Innocenti C 1999 *J. Fluid Mech.* **393** 123
[63] Celani A, Cencini M, Vergassola M, Vincenzi D and Villermaux E 2004 *J. Fluid Mech.* submitted
[64] Shraiman B I and Siggia E D 1998 *Phys. Rev.* E **57** 2965
[65] Pumir A 1998 *Phys. Rev.* E **57** 2914
[66] Castiglione P and Pumir A 2001 *Phys. Rev.* E **64** 056303
[67] Gat O, L'vov V S and Procaccia I 1997 *Phys. Rev.* E **56** 406